Chaos in Homeostatically Regulated Neural Systems

Wilten Nicola *[1], Peter John Hellyer[1], Sue Ann Campbell[2], and Claudia Clopath[1]

[1]Department of Bioengineering, Imperial College London, London, United Kingdom, SW7 2AZ
[2]Department of Applied Mathematics, University of Waterloo, 200 University Avenue W., Waterloo, Ontario, Canada, N2L 3G1

June 7, 2018

Abstract

Low-dimensional yet rich dynamics often emerge in the brain. Examples include oscillations and chaotic dynamics during sleep, epilepsy, and voluntary movement. However, a general mechanism for the emergence of low dimensional dynamics remains elusive. Here, we consider Wilson-Cowan networks and demonstrate through numerical and analytical work that homeostatic regulation of the network firing rates can paradoxically lead to a rich dynamical repertoire. The dynamics include mixed-mode oscillations, mixed-mode chaos, and chaotic synchronization when the homeostatic plasticity operates on a moderately slower time scale than the firing rates.. This is true for a single recurrently coupled node, pairs of reciprocally coupled nodes without self-coupling, and networks coupled through experimentally determined weights derived from functional magnetic resonance imaging data. In all cases, the stability of the homeostatic set point is analytically determined or approximated. The dynamics at the network level are directly determined by the behavior of a single node system through synchronization in both oscillatory and non-oscillatory states. Our results demonstrate that rich dynamics can be preserved under homeostatic regulation or even be caused by homeostatic regulation.

Lead Paragraph

When recordings from the brain are analyzed, rich dynamics such as oscillations or low-dimensional chaos are often present. However, a general mechanism for how these dynamics emerge remains unresolved. Here, we explore the potential that these dynamics are caused by an interaction between synaptic homeostasis, and the connectivity between distinct populations of neurons. Using both analytical and numerical approaches, we analyze how data derived connection weights interact with inhibitory synaptic homeostasis to create rich dynamics such chaos and oscillations operating on multiple time scales. We demonstrate that these rich dynamical states are present in simple systems such as single population of neurons with recurrent coupling. The dynamics of these simple systems are directly inherited in large networks while properties of the coupling matrices determine when these rich dynamics emerge as a function of the parameters of the neuronal populations. Indeed, we find that the removal of single nodes or connections can substantially alter where these rich dynamics onset in the parameter space.

1 Introduction

The human brain contains billions of neurons each receiving potentially thousands of connections from their neighbours. Despite this complexity, low-dimensional dynamics often appear in the brain in different regions and contexts. Examples include oscillations such as the theta and gamma oscillations in the hippocampus [Buzsáki, 2002, Buzsáki and Wang, 2012, Buzsáki et al., 2012], low dimensional oscillatory dynamics during grasping and other motions [Churchland et al., 2012], or even low dimensional chaotic dynamics during epileptic

---

*Corresponding Author: w.nicola@imperial.ac.uk

seizures and different sleep phases [Babloyantz and Destexhe, 1986]. These dynamics are sometimes pathological, such as during epileptic seizures while other times they are functional, such as during sleep states. Despite the low-dimensionality, the dynamics these systems display are often complex [Babloyantz and Destexhe, 1986]. However, a general mechanism as to how these dynamical regimes might emerge remains elusive.

If these dynamical regimes are learned and not inherited, then plasticity in the synaptic weights that couple neurons together is necessary. For many neural circuits, strong evidence exists for a form of homeostatic plasticity [Froemke et al., 2007, Frank et al., 2006, Bacci et al., 2001, Turrigiano and Nelson, 2004]. The function of homeostatic plasticity is to prevent run-away excitation in the circuit and thus prevent pathological states such as epileptic seizures. Additionally, homeostatic plasticity prevents a catastrophic loss of neuronal activity which results in network quiescence. In other words, homeostatic plasticity serves to maintain a stable background firing rate.

Recent modeling work has demonstrated a novel inhibitory homeostatic plasticity mechanism designed to regulate activity [Vogels et al., 2011]. This mechanism works by applying slow variations in the synaptic weights from the inhibitory neurons to the excitatory neurons [Vogels et al., 2011]. As the excitatory neurons start firing in excess of their homeostatic set points, the synaptic weights from the inhibitory neurons increase in strength to prevent run-away excitation. If the excitation in the network is too low, the inhibitory weights decrease in strength to disinhibit the excitatory neurons. The homeostatic mechanism can drive initially synchronized activity into the asynchronous irregular regime defined by variable spiking but with a constant time averaged firing rate [Vogels et al., 2011, Brunel, 2000].

These homeostatic mechanisms fundamentally exist to stabilize network dynamics to an equilibrium point [Turrigiano and Nelson, 2004]. Indeed, they exist as a counter mechanism to offset the often destabilizing effects of Hebbian plasticity [Turrigiano and Nelson, 2004]. Thus, it is surprising to consider homeostasis to be the potential source of complex dynamical systems. However, recent work on different forms of homeostatic plasticity demonstrate the rich dynamical repertoire that networks regulated by homeostatic plasticity can display [Udeigwe et al., 2017, Zenke et al., 2013, Harnack et al., 2015, Hellyer et al., 2016]. For example, a coupled Wilson-Cowan system with inhibitory homeostatic synaptic plasticity and excitatory weights estimated from diffusion spectrum imaging data showed rich spontaneous dynamics such as neural avalanches [Hellyer et al., 2016]. However, it is difficult to determine what the source of the rich dynamical repertoire in the system considered in [Hellyer et al., 2016] is as the underlying networks contain neuronal noise, synaptic transmission delays, non-smooth dynamics, and complex coupling. All four components may be the source of complex dynamics.

In this work, we attempt to disentangle the effect of the homeostatic dynamics by analyzing a smooth Wilson-Cowan ([Wilson and Cowan, 1972]) system similar to the system numerically analyzed in [Hellyer et al., 2016]. Here, we consider the system without delays or noise as both conditions can increase the complexity of otherwise simple network dynamics. We show that the rich dynamics can arise from inhibitory synaptic homeostasis alone. Indeed, complex dynamics arise in a single node with recurrent excitation and homeostatically regulated inhibition. For example, the single node system displays a period doubling cascade to chaos, mixed-mode oscillations, and mixed-mode chaos. Furthermore, we demonstrate that these results also occur in coupled dual node systems, and in large coupled node systems. The coupling in the large network is identical to the connectivity considered in [Hellyer et al., 2016] and derived from functional magnetic resonance imaging data from [Hagmann et al., 2008, Honey et al., 2009]. For both cases, we find that the complex dynamics of the single node carry over to higher dimensions. Finally, we consider node and connection deletion in simulations using the data derived coupling matrices. We find that the homeostatic effect on firing rate stability is substantially boosted by the deletion of very specific nodes or connections in the network.

2 The Wilson-Cowan System With Homeostatic Regulation

The system of equations we consider model the average activity of a population of neurons phenomenologically [Wilson and Cowan, 1972]. The population consists of subpopulations of excitatory neurons, E, and inhibitory neurons, I. Each population corresponds to a single equation. For example, a single recurrently coupled population of excitatory and inhibitory neurons are governed by the following dynamical system:

$$\tau_E E' = -E + \phi\left(W^{EE}E - W^{EI}I\right) \quad (1)$$

$$\tau_I I' = -I + \phi\left(W^{IE}E\right) \quad (2)$$

The coupling terms W^{EE}, W^{EI}, W^{IE} are all assumed to be positive scalars while the self-inhibition term is assumed to be zero, for simplicity. The function $\phi(x)$ is a sigmoidal transfer function that transforms the net current arriving at a population into the population activity. The time constants τ_E and τ_I denote time scales of the excitatory and inhibitory populations, respectively. The equations (1)-(2) are more commonly referred to as the Wilson-Cowan system [Wilson and Cowan, 1972]. Here, we also consider the homeostatic modification from [Vogels et al., 2011, Hellyer et al., 2016]:

$$\tau_W W^{EI'} = I(E-p) \tag{3}$$

Equation (3) alters the dynamics of the inhibitory synaptic weight in order to drive the excitatory population toward p, the homeostatic set point of the network. Equations (1)-(3) together define the dynamics of a single, recurrently coupled node. As we will see in Section 3, analyzing the single node system is vital towards understanding the dynamics of the large network.

The network equations are given by the following:

$$\begin{aligned}
\tau_E E_k' &= -E_k + \phi\left(\sum_{i=1}^{N} W_{ik}^{EE} E_i - W_k^{EI} I_k\right) && (4)\\
\tau_I I_k' &= -I_k + \phi(W_k^{IE} E_k) && (5)\\
\tau_W W_k^{EI'} &= I_k(E_k - p) && (6)
\end{aligned}$$

The excitatory activity of population k is given by E_k while the inhibitory activity is given by I_k for $k = 1, 2, \ldots N$. These nodes are coupled by the potentially long range weight projection matrix $\boldsymbol{W}^{EE}$ while a node inhibits itself through the diagonal weight matrix $\boldsymbol{W}^{EI}$. We assume that no long-range inhibition is possible, hence the diagonal nature of $\boldsymbol{W}^{EI}$. Furthermore, we will assume that a node can only excite its own inhibitory population, and thus $\boldsymbol{W}^{IE}$ is also diagonal.

The time constants for the excitatory and inhibitory population activities, and inhibitory homeostatic synaptic weight are given by τ_E, τ_I, and τ_W, respectively. In this work, we will primarily consider the case where $\tau_W \gg \tau_E, \tau_W \gg \tau_I$ with $\tau_W = 5\tau_E$, $\tau_E = \tau_I = 1$ for the majority of numerical simulations. The excitation and inhibition operate on the same time scale, while the homeostasis operates on a slower time scale. Here, we consider the case where the plasticity operates on a slower time scale, however the separation of time scales is moderate. This smaller separation is due to the Wilson-Cowan system phenomenologically representing the activity or average firing of a population of neurons, and firing rates can have significantly slower dynamics than the neuronal dynamics that constitute a network. This can be caused for example by short-term plasticity ([Markram and Tsodyks, 1996, Stevens and Wang, 1995]), spike-frequency adaptation ([Benda and Herz, 2003]), or clustered coupling between the individual neurons that constitute a node ([Litwin-Kumar and Doiron, 2012]). However, we analyze the system more generally when we consider the origin of Canards and mixed-mode oscillations in Section 3 and consider stronger separations of the time scales numerically to determine if the resulting network dynamics are robust.

The transfer function $\phi(x)$ is a smooth sigmoid function which we will constrain to satisfy the following properties:

$$\begin{aligned}
\phi'(x) &> 0, \forall x && (7)\\
\lim_{x\to\infty} \phi(x) &= 1 && (8)\\
\lim_{x\to-\infty} \phi(x) &= 0 && (9)
\end{aligned}$$

While much of our derivations and analysis are general for sigmoid functions that satisfy (7)-(9), we consider the logistic function:

$$\phi(x) = \frac{1}{1+\exp(-ax)}, \quad \phi'(x) = a\phi(x)(1-\phi(x)), \quad \phi^{-1}(x) = \frac{1}{a}\log\left(\frac{y}{1-y}\right) \tag{10}$$

for numerical applications. The parameter a determines the steepness of the sigmoid. While $\phi(x)$ is a smooth sigmoid function, other transfer functions are also possible. In particular, non-smooth variants of $\phi(x)$ can also be considered which impact the final dynamics of the network [Harris and Ermentrout, 2015, Nicola and Campbell, 2016]. We leave this for future work.

To simplify the notation further, we will rescale time with $\hat{t} = \tau_I t$. For the single node, this yields the following system:

$$\begin{aligned}
\tau_1 E' &= -E + \phi(W^E E - W^I I) && (11)\\
I' &= -I + \phi(\theta E) && (12)\\
\tau_2 W^{I'} &= I(E-p). && (13)
\end{aligned}$$

with $\tau_1 = \tau_E/\tau_I$, $\tau_2 = \tau_W/\tau_I$. For simplicity, we will relabel the scalar parameters in the single and dual node cases with W^E and W^I for EE and EI synaptic weights and θ for the IE synaptic weight. Finally, the coupling matrix for the large network, $\boldsymbol{W}^{EE}$, is derived from functional neural imaging data (see [Hellyer et al., 2016, Hagmann et al., 2008, Honey et al., 2009] for further details). These data-derived coupling matrices have no self-coupling between nodes ($\boldsymbol{W}_{ii}^{EE} = 0$). This would seem to imply that analysis of the single system driven by self coupling given by equations (1)-(3) will not help in understanding the dynamics of the full network where $W_{ii}^{EE} = 0, \forall i$. However, as we will see the symmetric double-node system without self-coupling:

$$
\begin{aligned}
\tau_1 E_1' &= -E_1 + \phi(W^E E_2 - W_1^I I_1) && (14)\\
I_1' &= -I_1 + \phi(\theta E_1) && (15)\\
\tau_2 W_1^{I\prime} &= I_1(E_1 - p) && (16)\\
\tau_1 E_2' &= -E_2 + \phi(W^E E_1 - W_2^I I_2) && (17)\\
I_2' &= -I_2 + \phi(\theta E_2) && (18)\\
\tau_2 W_2^{I\prime} &= I_2(E_2 - p) && (19)
\end{aligned}
$$

has largely identical dynamics to the single-node system and in fact synchronizes to solutions of the single-node system.

We structure the paper as follows: In Section 3 we analyze the single-node system and demonstrate that the majority of the rich dynamics we see for both the dual node and the full network are present for the single node. In Section 4 we numerically demonstrate that the dual node system without self-coupling synchronizes to the single node system analyzed in Section 4. Finally, in Section 5, we simulate and analyze the full network equations demonstrating a direct inheritance of their dynamics from the single node system. The parameter values we consider for all systems are shown in Table 1, unless otherwise specified as a bifurcation parameter (see figure captions).

3 Single Node Analysis

3.1 Local Analysis

Due to the homeostatic mechanism in equation (3), only one equilibrium exists and is determined by the following equations:

$$\overline{E} = p, \quad \overline{I} = \phi(\theta p), \quad \overline{W^I} = \frac{W^E p - \phi^{-1}(p)}{\phi(\theta p)}$$

which is valid for $p \in (0, 1)$. We will subsequently refer to this equilibrium as $\bar{\boldsymbol{x}} = (\overline{E}, \overline{I}, \overline{W^I})$. As $W^I > 0$ we require:

$$W^E p > \phi^{-1}(p).$$

This sets a range on the admissable values of W^E allowed as a function of p, in addition to the constraint that $W^E > 0$. Note that if $\phi^{-1}(p) = 0$, then we can consider all $W^E > 0$. For our sigmoid (10), this implies that we require $p < 0.5$.

After some simplification, the Jacobian of this system is given by

$$J = \begin{pmatrix} -\frac{1}{\tau_1} + \frac{\phi'(\phi^{-1}(p))W^E}{\tau_1} & -\frac{\overline{W^I}\phi'(\phi^{-1}(p))}{\tau_1} & -\frac{\overline{I}\phi'(\phi^{-1}(p))}{\tau_1} \\ \phi'(\theta p)\theta & -1 & 0 \\ \frac{\overline{I}}{\tau_2} & 0 & 0 \end{pmatrix}.$$

Which yields the following characteristic polynomial for the single node system:

$$
\begin{aligned}
C_{SN}(\lambda) \;=\; & \lambda^3 + \lambda^2\left(\frac{1 - W^E\phi'(\phi^{-1}(p))}{\tau_1} + 1\right) + \lambda\left(\frac{1 - W^E\phi'(\phi^{-1}(p))}{\tau_1} + \frac{\overline{W^I}\phi'(\phi^{-1}(p))\phi'(\theta p)\theta}{\tau_1} + \frac{\overline{I}^2\phi'(\phi^{-1}(p))}{\tau_1\tau_2}\right)\\
& + \frac{\overline{I}^2\phi'(\phi^{-1}(p))}{\tau_1\tau_2}.
\end{aligned}
$$

The determinant of the Jacobian is given by

$$\det J = \lambda_1\lambda_2\lambda_3 = -\frac{\overline{I}^2\phi'(\phi^{-1}(p))}{\tau_1\tau_2} = -\frac{\phi(\theta p)^2\phi'(\phi^{-1}(p))}{\tau_1\tau_2} < 0.$$

As the determinant is always negative, this limits the dynamical repertoire of this system due to the homeostatic variable. Indeed, due to the dynamics of W^I, aside from $(\overline{E}, \overline{I}, \overline{W^I})$, no other equilibria exist and thus local bifurcations that create or destroy equilibria via $\lambda = 0$ crossings are not possible. This implies that no bistability in equilibria is possible, as in other classical Wilson-Cowan systems. Thus, we can attempt to look for Hopf bifurcations. Furthermore, as the system is cubic and the determinant is negative, one of the eigenvalues is always negative. This corresponds to the existence of a stable manifold for the equilibrium globally in the parameter space. The other eigenvalues must both be real and of the same sign, or complex. Further, using the Routh-Hurwitz criterion, one can show that all roots of the characteristic equation have negative real part if $1 - W^E\phi'(\phi^{-1}(p)) > 0$.

To determine the potential loss of stability due to Hopf-bifurcations, substitution of the Hopf-bifurcation condition $\lambda = i\omega$ into the characteristic polynomial yields the following:

$$\begin{aligned} 0 &= -i\omega^3 - \omega^2\left(\frac{1 - W^E\phi'(\phi^{-1}(p))}{\tau_1} + 1\right) + i\omega\left(\frac{1 - W^E\phi'(\phi^{-1}(p))}{\tau_1} + \frac{\overline{W^I}\phi'(\phi^{-1}(p))\phi'(\theta p)\theta}{\tau_1} + \frac{\overline{I}^2\phi'(\phi^{-1}(p))}{\tau_1\tau_2}\right) \\ &+ \frac{\overline{I}^2\phi'(\phi^{-1}(p))}{\tau_1\tau_2}, \end{aligned}$$

which after equating real and imaginary parts yields

$$\begin{aligned} 0 &= \omega^3 - \omega\left(\frac{1 - W^E\phi'(\phi^{-1}(p))}{\tau_1} + \frac{\overline{W^I}\phi'(\phi^{-1}(p))\phi'(\theta p)\theta}{\tau_1} + \frac{\overline{I}^2\phi'(\phi^{-1}(p))}{\tau_1\tau_2}\right) \\ 0 &= \omega^2\left(\frac{1 - W^E\phi'(\phi^{-1}(p))}{\tau_1} + 1\right) - \frac{\overline{I}^2\phi'(\phi^{-1}(p))}{\tau_1\tau_2}. \end{aligned}$$

Solving for ω as a function of the network parameters yields:

$$\omega = \sqrt{\frac{1 - W^E\phi'(\phi^{-1}(p))}{\tau_1} + \frac{\overline{W^I}\phi'(\phi^{-1}(p))\phi'(\theta p)\theta}{\tau_1} + \frac{\overline{I}^2\phi'(\phi^{-1}(p))}{\tau_1\tau_2}}.$$

The Hopf bifurcation curve is implicitly defined by

$$\begin{aligned} 0 &= \left(\frac{1 - W^E\phi'(\phi^{-1}(p))}{\tau_1} + \frac{\overline{W^I}\phi'(\phi^{-1}(p))\phi'(\theta p)\theta}{\tau_1} + \frac{\overline{I}^2\phi'(\phi^{-1}(p))}{\tau_1\tau_2}\right)\left(\frac{1 - W^E\phi'(\phi^{-1}(p))}{\tau_1} + 1\right) \\ &- \frac{\overline{I}^2\phi'(\phi^{-1}(p))}{\tau_1\tau_2} \end{aligned} \tag{20}$$

Defining the following quantities

$$\begin{aligned} \mu &= \frac{1 - W^E\phi'(\phi^{-1}(p))}{\tau_1} \\ F(\theta) &= \frac{1 - p^{-1}\phi^{-1}(p)\phi'(\phi^{-1}(p))}{\tau_1} \\ \kappa(\theta) &= \frac{p\phi'(\theta p)\theta}{\phi(\theta p)} \\ D(\theta) &= \frac{\overline{I}^2\phi'(\phi^{-1}(p))}{\tau_1\tau_2}, \end{aligned}$$

then the Hopf bifurcation condition can be written as a quadratic equation in μ. Solving for μ yields

$$\mu_\pm = \frac{-(D(\theta) + F(\theta)\kappa(\theta) + 1 - \kappa(\theta)) \pm \sqrt{(F(\theta)\kappa(\theta) + D(\theta) + 1 - \kappa(\theta))^2 - 4\kappa(\theta)F(\theta)(1 - \kappa(\theta)}}{2(1 - \kappa(\theta))}.$$

Only the positive branch of μ yields a Hopf-bifurcation as we require $\omega^2 > 0$, which after rearranging the Hopf bifurcation condition (20) yields:

$$\begin{aligned} \omega_\pm^2 &= \frac{D(\theta)}{\mu_\pm + 1} \\ \mu_- + 1 &= \frac{-(D(\theta) + F(\theta)\kappa(\theta) - (1 - \kappa(\theta))) - \sqrt{(D(\theta) + F(\theta)\kappa(\theta) - (1 - \kappa(\theta))^2 + 4D(\theta)(1 - \kappa(\theta)))}}{2(1 - \kappa(\theta))} \end{aligned}$$

which implies that $\mu_- < 0$ is thus an inadmissable solution for a Hopf-bifurcation while μ_+ is an admissable under the sufficient condition

$$\kappa(\theta) = \frac{p\phi'(\theta p)\theta}{\phi(\theta p)} < 1 \tag{21}$$

By considering the properties of the sigmoid function $\phi(x)$, a routine derivation shows that the inequality (21) holds when $a\theta p < ((1-\phi(\theta p))^{-1}$ which is always valid as:

$$a\theta p < \frac{1}{1-\phi(\theta p)} = 1 + \exp(a\theta p)$$

and $z < 1 + \exp(z)$ for all z. The final Hopf bifurcation curve is given by:

$$W^E_{Hopf}(\theta) = \frac{1}{\phi'(\phi^{-1}(p))}\left(1 - \tau_1\mu_+(\theta)\right). \tag{22}$$

in the (θ, W^E) parameter space.

Given the fact that we can explicitly solve for the Hopf-bifurcation curve, we can simulate in its vicinity to determine the resulting behavior of the single-node system. Direct numerical simulation in addition to numerical continuation using XPPAUT (not shown) indicate that the Hopf bifurcation is likely supercritical, as stable limit cycles emerge for $W^E > W^E_{Hopf}(\theta)$ (Figure 1, 1A). Computing the first Lyapunov coefficient is cumbersome for the full-3D system as it requires a center manifold reduction. However, for $\theta = 0$ case, one can prove that the Lyapunov coefficient is strictly negative (see Appendix A). Thus, we should expect that the first Lyapunov exponent is negative for small θ which suggests a supercritical Hopf bifurcation.

Finally, taking the limits $\theta \to 0$ or $\theta \to \infty$ yields

$$W^E_{Hopf}(0) = W^E_{Hopf}(\infty) = \frac{1}{\phi'(\phi^{-1}(p))} \tag{23}$$

with $W^E_{Hopf}(\theta) \geq W^E_{Hopf}(0)$. The inequality can be proven by considering that $F(\theta) \geq 0$, $\mu_+(\theta) \leq 0$ where equality only occurs in the asymptotic limits considered in (23). The value $W^E_{Hopf}(0)$ is the critical value after which synaptic homeostasis can no longer guarantee stability of the equilibrium $\bar{\boldsymbol{x}}$. After this value, depending on the strength of the excitatory to inhibitory coupling θ, stability is lost through a supercritical Hopf bifurcation. This is however not a catastrophic bifurcation, and thus near the onset of the Hopf bifurcation we are still confined to a neighbourhood around $\bar{\boldsymbol{x}}$. Note that for the sigmoid (10) we consider, $W^E_{Hopf}(0) = \frac{1}{ap(1-p)}$, which implies that smoother sigmoids (small a) yield a larger parameter region of homeostatic control.

3.2 Period Doubling Cascade to Chaos Followed by a Pinching of the Tent Map

For larger values of W^E, the system displays chaotic activity which was verified by computing the maximum Lyapunov exponent numerically (Figure 2). This chaotic attractor contains small excursions from $\bar{\boldsymbol{x}}$. Again, in this region the homeostatic mechanism is still operating within some degree of tolerance as the chaotic attractor is contained within small neighbourhood of the equilibrium. Mixed mode oscillations are also present past the Hopf-bifurcation (Figure 1C). Surprisingly, for large enough values of W^E, the chaotic attractor can also contains components that operate on two separate time scales (Figure 1D). This is referred to as "mixed mode chaos" [Desroches et al., 2012, Koper, 1995]

Given the exotic nature of the mixed mode-chaos in this system, we investigated how chaos emerges in this system. First, we fixed θ and steadily increased W^E and observed a classical period doubling cascade (Figure 2A,2B) to chaos. Numerically computing the maximal Lyapunov exponent ([Sprott and Sprott, 2003]) over the two parameter (θ, W^E) region reveals a contiguous region of chaotic solutions above the Hopf bifurcation curve (Figure 2C).

For smaller values of $W^E > W^E_{Hopf}$, the chaotic solutions are classical in nature (2D). For example, by plotting the kth maxima of the E variable, E^*_k as a function of E^*_{k-1}, we find a stereotypical unimodal peak-to-peak or tent map [Lorenz, 1963, Strogatz, 2014] (Figure 2E). However, as we increase W^E further, a pseudo-singularity or "pinch" emerges in the tent map at the location of the former maximum. This is not a true singularity of this map as the set $E \in (0,1)$ is invariant. The emergence of this singularity in the tent map corresponds to the emergence of mixed-mode chaos. However, mixed mode chaos occurs over a narrow parameter regime for the single node. For larger values of $W^E \gg W^E_{Hopf}(\theta)$, the system only displays large relaxation limit cycle solutions.

Finally, we remark that period doubling cascades and mixed mode behaviors are preserved under larger separations of time scales, up to approximately $\tau_W = 200\tau_E$, $\tau_E = \tau_I$ (Figure 2F). Thus, even for significantly larger separations of time scales, the Hopf bifurcation induced by the homeostatic coupling leads to the emergence of complex, yet low dimensional dynamics.

3.3 Canards and Mixed Mode Oscillations

Next, we investigated how mixed-mode oscillations emerge in the three-dimensional, single-node case. In particular, recent analytical work has demonstrated several cases through which mixed-mode oscillations can emerge in a three-dimensional system exhibiting different separations of time scales. Examples include folded singularities involving one fast variable and two slow variables, or the "tourbillon" case involving two fast variables and one slow dynamical variable, singular-Hopf bifurcations, and systems exhibiting three different time scales. [Wechselberger, 2005, Krupa and Wechselberger, 2010, Vo and Wechselberger, 2015, Desroches et al., 2012]. These systems can give rise to mixed-mode oscillations through different mechanisms.

As our system has two fast variables and one slow variable, we hypothesized that the most likely mechanism for the emergence of mixed-mode oscillations for our network equations was the so called tourbillon case [Desroches et al., 2012]. This is due to the presence of two fast variables (E, I) in addition to the slow weight W^I. However, the mixed-mode oscillations cannot arise from the tourbillon case in our system. Indeed, this requires that the fast variables, given by:

$$\tau_1 E' = -E + \phi\left(W^E E - W^I I\right) \qquad (24)$$

$$I' = -I + \phi\left(\theta E\right) \qquad (25)$$

undergo a Hopf bifurcation [Desroches et al., 2012]. While Hopf bifurcations are possible in this system, they do not seem to be linked to MMOs, at least for the parameters we consider. The Hopf bifurcations occur far from the region in parameter space where MMOs occur and were never observed to be associated with stable limit cycles.

With the tourbillon case likely removed as a possible cause of mixed-mode oscillations, we are left with several other possibilities explored in the literature. These include the folded singularities, three time-scale systems, or singular-Hopf bifurcations ([Desroches et al., 2012]. The time scales in our network are given by $\tau_E/\tau_I = 1$, $\tau_W/\tau_I = 5$. Unfortunately, all other possibilities that are currently explored in the literature require either two slow time scales, or three separate time scales [Desroches et al., 2012]. For the nominal parameter values we have considered, our system has one slow variable and two identically fast variables.

However, an alternate possibility is that the mixed-mode oscillations are born in alternate time scale limits, yet persist as the time-scale conditions are relaxed. For example, these mixed-mode oscillations may be due to folded-nodes or folded-saddles for $\tau_W = \tau_I \gg \tau_E$ or singular Hopf bifurcations in the same limit, or the three time-scale limit $\tau_W \gg \tau_I \gg \tau_E$, all of which have been recently summarized in [Desroches et al., 2012]. As $\tau_I \to O(\tau_E)$, the mixed mode solutions born in the limit that $\tau_I \gg \tau_E$ persist past this limit.

First, we considered folded singularities as these cases were the most promising. Mixed mode oscillations arising from a folded singularities (either folded saddles or folded nodes) occur when the system has one fast variable and two slow variables. Both folded node and folded saddles can have canard solutions [Desroches et al., 2012]. These systems are often generalizations of the canard solutions one observes in simple two-dimensional systems such as the Van der Pol system.

We note that canards exist over a exponentially small parameter regime in two-dimensional reductions of the recurrently coupled single node system. For example, the E, W^I system with I either set to $\phi(\theta E)$ (Figure 3A) or $I = \frac{1}{2}$, in the limit that $\theta = 0$ (not shown) both have canard solutions. Further, we prove in Appendix B for the $\theta = 0$ case that the two-dimensional system:

$$E' = -E + \phi(W^E E - W^I) \qquad (26)$$

$$W^{I\prime} = \epsilon(E - p) \qquad (27)$$

analytically has a canard point. This is due to the cubic-like nature of the critical manifold of (26), which is preserved as a folded surface in 3D. The system (26)-(27) is arrived by a suitable rescaling of time and space, after setting $\theta = 0$ thereby uncoupling the inhibition from the other dynamics and rendering the dynamics of the inhibitory variable a stable manifold.

Further, if we consider the full 3D single-recurrently coupled node system, the null-surfaces for the excitatory fast variable are indeed folded and contain two attracting regions and a repelling region. The dynamics for large amplitude oscillations follow the attracting components of the null-surface. This numerical analysis suggest that the mixed-mode oscillations might arise from folded singularities in a relaxed parameter regime.

Thus, we conducted the folded singularity analysis in [Desroches et al., 2012, Wechselberger, 2005] and determined where in the (θ, W^E) parameter region we would expect folded singulairites (see Appendix B) and their resulting nature. We found both folded-node and folded saddle regions (Figure 3D). Interestingly, we numerically found these regions to be separated by the Hopf-bifurcation curve. Furthermore, we ran numerical simulations for $\tau_W = \tau_I = 100\tau_E$ and automatically classified solutions as having mixed-mode elements (Figure 3D). Here, we found that over a large region in the analytically predicted folded-saddle space, mixed mode oscillations existed (Figure 3D,E). We also remark here that the critical manifold for the single node system has some pathological properties that might render local analysis less useful. In particular, the folded surface is parameterized by

$$S = \left\{ (E, I, W^I) : (E, I) \in (0,1) \times (0,1), W^I = \frac{W^E E - \phi^{-1}(E)}{I} \right\}$$

where $\phi^{-1}(E) = -\frac{1}{a}\log\left(\frac{1-E}{E}\right)$. Thus, the critical manifold diverges at $E = 0, 1$, or $I = 0$.

Thus, Canards analytically exist (through a Canard point) for the 2D reduced system under the limit that $\theta \to 0$, while the 3D system in the limit that $\tau_I = \tau_W \gg \tau_E$ exhibits certain characteristics of a potential folded-singularity. We numerically found the the Hopf-bifurcation curve was a good predictor for the boundary between the folded-node and folded-saddle regions. This might be indicative of the folded saddle-node of type II/singular Hopf bifurcation where Hopf-bifurcations of the full-system exist near the transition of a folded-saddle to a folded-node due to an equilibrium collision with a fold of the critical manifold.

4 The Dual-Node Case: Synchronous Solutions to the Single Node

As the large network equations contain no self coupling in the $\boldsymbol{W}^{EE}$ weight matrix (diag($\boldsymbol{W^{EE}}$) = $\boldsymbol{0}$), the single-node analysis that we have conducted is not necessarily informative of the large network dynamics. Thus, analysis must be conducted on the simplest possible system without self-coupling, the dual-node reciprocally coupled system given by equations (14)-(19). In this system, the local homeostatic mechanism attempts to stabilize the excitatory activity while the opposing node functions to stimulate their neighbour.

First, we conducted numerical simulations of the dual-node system to determine what dynamical behaviors are possible. Surprisingly, we found that over all parameter regimes tested, the dual-node system without self-coupling synchronizes to solutions of the single-node, recurrently coupled system (Figure 4A,B). For example, the dual-node system asymptotically tends towards the same chaotic attractors, limit cycles, and mixed mode solutions as the single node system (Figure 4A). For oscillatory solutions, this is not surprising as a simple derivation shows that any stable solution of the single-node system potentially corresponds to a synchronous solution in the dual-node system. For chaotic attractors, the dual-node system exhibits a case of synchronized chaos when the parameters for both nodes are identical [Pecora and Carroll, 1990].

4.1 Local Stability Analysis of Equilibria

Again, due to the homeostatic nature of the dual-node system, the only equilibrium that exists is given by equation

$$\overline{E}_1 = \overline{E}_2 = p, \quad \overline{I}_1 = \overline{I}_2 = \phi(\theta p), \quad \overline{W^I}_1 = \overline{W^I}_2 = \frac{W^E p - \phi^{-1}(p)}{\phi(\theta p)}.$$

Furthermore, using the Jacobian to solve for the characteristic polynomial yields the following:

$$C_{DN}(\lambda) = C_{SN}(\lambda) Q(\lambda) \tag{28}$$

$$Q(\lambda) = \lambda^3 + \lambda^2 \left(\frac{1 + W^E \phi'(\phi^{-1}(p))}{\tau_1} + 1 \right) + \lambda \left(\frac{1 + W^E \phi'(\phi^{-1}(p))}{\tau_1} + \frac{\overline{W^I} \phi'(\phi^{-1}(p)) \phi'(\theta p)\theta}{\tau_1} + \frac{\overline{I}^2 \phi'(\phi^{-1}(p))}{\tau_1 \tau_2} \right) + \frac{\overline{I}^2 \phi'(\phi^{-1}(p))}{\tau_1 \tau_2}. \tag{29}$$

Thus, instability in $C_{SN}(\lambda)$ implies instability in the dual-node system for any equilibria. Furthermore, by the Routh-Hurwitz criterion [Wiggins, 2003], all roots of $Q(\lambda)$ lie in the left complex plane if:

$$\left(\frac{1 + W^E \phi'(\phi^{-1}(p))}{\tau_1} + 1 \right) \left(\frac{1 + W^E \phi'(\phi^{-1}(p))}{\tau_1} + \frac{\overline{W^I} \phi'(\phi^{-1}(p)) \phi'(\theta p)\theta}{\tau_1} + \frac{\overline{I}^2 \phi'(\phi^{-1}(p))}{\tau_1 \tau_2} \right) > \frac{\overline{I}^2 \phi'(\phi^{-1}(p))}{\tau_1 \tau_2}.$$

For all physical solutions, the inequality is satisfied as the term $\frac{\bar{I}^2\phi'(\phi^{-1}(p))}{\tau_1\tau_2}$ can be subtracted from both sides of (30) with all the remaining terms on the right hand side being strictly positive. However, roots on the right-complex plane may occur for non-physical values of these coefficients, for example when the weights are negative. This analysis implies that for all permissible (physical) equilibria, the stability of the dual node system is directly inherited from the stability of the single node. In other words, for symmetrically coupled systems, the local homeostasis rule loses no robustness in regulating network dynamics up to the Hopf-bifurcation and the recurrent inhibition can counteract non-local excitation just as well as local excitation.

4.2 Stability Analysis of Limit Cycles

If we consider any limit cycle for the single node-system $\boldsymbol{x}(t) = (E(t), I(t), W^I(t))$ such that $\boldsymbol{x}(t) = \boldsymbol{x}(t+T)$ for some $T > 0$, $\forall t$, then the following is an admissable limit cycle solution to the dual-node system:

$$\boldsymbol{z}(t) = \begin{pmatrix} \boldsymbol{x}(t) \\ \boldsymbol{x}(t) \end{pmatrix}$$

with an identical period T, for all $t > 0$. Furthermore, if we consider the monodromy matrix system

$$\dot{\boldsymbol{\epsilon}} = A(\boldsymbol{x}(t))\boldsymbol{\epsilon} \tag{30}$$

derived by linearizing equations (1)-(3) around $\boldsymbol{x}(t)$ then linearization for equations (14)-(19) can be written as

$$\begin{aligned} \dot{\boldsymbol{\epsilon}} &= A(\boldsymbol{x}(t))\boldsymbol{\epsilon} + g_\epsilon(\boldsymbol{\epsilon}, \boldsymbol{x}(t)) \qquad (31) \\ \dot{\boldsymbol{\nu}} &= A(\boldsymbol{x}(t))\boldsymbol{\nu} + g_\nu(\boldsymbol{\epsilon}, \boldsymbol{x}(t)). \qquad (32) \end{aligned}$$

where

$$\begin{aligned} g_\epsilon(\boldsymbol{\epsilon}(t), \nu(t)) &= [W^E\phi'(W^E E(t) - I(t)W^I(t))(\nu_1(t) - \epsilon_1(t)), 0, 0]^T \\ g_\nu(\boldsymbol{\epsilon}(t), \nu(t)) &= [W^E\phi'(W^E E(t) - I(t)W^I(t))(\epsilon_1(t) - \nu_1(t)), 0, 0]^T \end{aligned}$$

In order to analyze the stability of limit cycles, we require a fundamental solution set to equations (31)-(32). First, if we consider the fundamental solution set for equation (30), $\boldsymbol{\Upsilon}(t) = [\boldsymbol{\epsilon}_1(t), \boldsymbol{\epsilon}_2(t), \boldsymbol{\epsilon}_3(t)]$, then three fundamental solutions of (31)-(32) are immediately given by $[\boldsymbol{\epsilon}_k(t), \boldsymbol{\epsilon}_k(t)]$ for $k = 1, 2, 3$. This implies that if the limit cycle is unstable in the single node system, (1)-(3), then it is unstable in the dual node system. We leave the stability analysis of these limit cycles and other trajectories for future work. We remark however that the recent work in [Coombes et al., 2018] analyzing the stability of limit cycles in piecewise neural mass models may be pertinent to resolving the stability of these limit cycles through Floquet analysis, under the assumption that the slope of the sigmoid is sharp ($a \to \infty$).

5 The Fully Coupled N-Node System

As we have previously demonstrated, the dual-node system without self coupling has identical dynamics to the single-node, self coupled system and even exhibits chaotic synchronization to identical attractors as the single-node. Thus, the single node is largely predictive of the qualitative dynamics of the coupled system despite the removal of self-coupling. Thus, we investigated if a similar result would apply to the large uncoupled system given by equations (4)-(6). First we analyzed a pair of analytically resolvable cases for matrices that satisfied specific assumptions. Then, we numerically explored the system (4)-(6) coupled by the weight matrix considered in [Hellyer et al., 2016].

5.1 Exactly Resolvable Cases

First, we considered a pair of analytically resolvable cases. If we consider the all-to-all coupled matrix:

$$\boldsymbol{W_{ij}^{EE}} = \begin{cases} \frac{W^E}{N_E - 1} & i \neq j \\ 0 & i = j \end{cases} \tag{33}$$

then there exist steady states $(E_j, I_j, W_j^I) = (p, \bar{I}, \bar{W}^I)$, $j = 1, 2, \ldots N$ given by the steady state formulas for the single and dual node systems. The characteristic polynomial reduces to:

$$C_{N_E}(\lambda) = \hat{Q}(\lambda)^{N_E - 1} C_{SN}(\lambda)$$

where $\hat{Q}(\lambda)$ and $C_{SN}(\lambda)$ are the polynomials resolved in the dual node (equation (29)) and single node case (See Appendix C). The polynomial $\hat{Q}(\lambda)$ however has $\bar{W^E} = \frac{W^E}{N-1}$ in place of W^E. Our previous analysis immediately applies and shows that with the coupling matrix (33), the system (4)-(6) has identical local stability to the single node. We refer to equation (33) as the "mean-field" assumption. Self-coupling need not be removed in this case, however the results will differ slightly from the single node if self-coupling is considered.

Finally, we remark that there is at least one other case where the stability of the system can be determined analytically, when the row sum of the coupling weight matrix is constant:

$$\sum_{j=1}^{N_E} \boldsymbol{W}_{ij}^{EE} = W^E, \quad i = 1, 2, \dots N_E$$

We decompose the weight matrix $\boldsymbol{W^{EE}} = W^E \cdot \boldsymbol{L}^{EE}$ where the row sum of $\boldsymbol{L}^{EE}$ is equal to one. The scalar term W^E scales the magnitude of the components of the weight matrix, similar to W^E in the single and dual node cases. For this case, one can resolve the eigenvalue spectrum explicitly as the characteristic polynomial factors readily:

$$C(\lambda) = \prod_{i=1}^{N_E}\left(\tilde{Q}(\lambda) - r_i\frac{\lambda(\lambda+1)\phi'(\phi^{-1}(p))}{\tau_1}W^E\right)$$

where each r_i is an eigenvalue of the weight matrix $\boldsymbol{L}^{EE}$. Each $\tilde{Q}(\lambda)$ is a cubic polynomial given by:

$$\hat{Q}(\lambda) = \lambda^3 + \lambda^2\left(\frac{1}{\tau_1}+1\right) + \lambda\left(\frac{1}{\tau_1} + \frac{\overline{W^I}\phi'(\phi^{-1}(p))\phi'(\theta p)\theta}{\tau_1} + \frac{\bar{I}^2\phi'(\phi^{-1}(p))}{\tau_1\tau_2}\right) + \frac{\bar{I}^2\phi'(\phi^{-1}(p))}{\tau_1\tau_2}. \tag{34}$$

The steady states $\bar{W^I}$ and $\bar{I}$ are given by identical formulas as in the single and dual node cases. Given the structure of the polynomial $Q(\lambda)$, this yields a Hopf-bifurcation immediately through an identical derivation in the single node case. The curve will be of the form:

$$W_{Hopf,i}^E(\theta) = \frac{1}{r_i\phi'(\phi^{-1}(p))}\left(1 - \tau_1\mu_+(\theta)\right) \tag{35}$$

where $\mu_+(\theta)$ is redefined and r_i is an eigenvalue of $\boldsymbol{L}$ (see Appendix C). As W^E is increased, the first intersection of $W^E = W_{Hopf,i}^E$ determines the Hopf bifurcation curve. For $\theta \gg 1$ and $\theta \ll 1$, this is readily seen to be the curve corresponding to the largest positive eigenvalue of $\boldsymbol{L}^{EE}$.

Additionally, if the row-sum of the matrix $\boldsymbol{W}^{EE}$ is non-constant, but narrowly distributed, one can still approximate the Hopf-bifurcation curve by using the mean-row sum (see Appendix C). We validate this approximation in the subsequent section as applied to the weight matrix considered in [Hellyer et al., 2016].

5.2 Numerical Exploration of the Experimentally Coupled System

The connectivity matrix, $\boldsymbol{W}^{EE} = \boldsymbol{W}^{EE}\cdot\boldsymbol{L}^{EE}$, is derived from functional neuroimaging data and is described in greater detail in [Hellyer et al., 2016, Honey et al., 2009, Hagmann et al., 2008]. The matrix $\boldsymbol{L}^{EE}$ is shown in Figure 5A. The matrix couples 66 homeostatically regulated Wilson-Cowan nodes. Furthermore, $\boldsymbol{L}_{ii}^{EE} = 0$ for all i and thus the nodes contain no self-coupling. As our single and dual node analyses indicate a branch of Hopf bifurcations, we numerically computed the eigenvalues over the two parameter (W,θ) space and searched for the first eigenvalue λ_i crossing $\mathrm{Re}(\lambda_i) = 0$ as a function of θ for each value of W. This yielded a similar potential Hopf-bifurcation curve as the single and dual node cases. The curve was again unimodal with identical asymptotes as $\theta \to 0$ and $\theta \to \infty$. We conducted large scale numerical simulations to determine if the curve indeed indicated a transition from steady state dynamics to oscillations. For $W < W_{Hopf}(\theta)$, we observe decay to a steady state equilibrium and oscillations or chaos for $W > W_{Hopf}(\theta)$ (Figure 5B,5C). Finally, we applied the analytical approximation derived in section 5.1 for comparison. The approximation has the greatest accuracy near the asymptotes $\theta \to 0$ and $\theta \to \infty$ and indicates that the common asymptotic behavior for W_{Hopf} is:

$$W_{Hopf}(\theta) \sim \frac{1}{\phi'(\phi^{-1}(p))r^{max}}, \quad \theta \to \infty, \theta \to 0$$

where r^{max} is the largest positive eigenvalue of $\boldsymbol{L}^{EE}$. As in our analysis of the single node, this asymptotic behavior corresponds to the region of guaranteed stability of the steady state for $W^E < W^E_{Hopf}(0)$

As in the single and dual node cases, the large network also displays mixed mode oscillations and mixed mode chaos (Figure 5C,D). Interestingly, due to the heterogeneous coupling in the weight matrix, the nodes do not all transition to chaotic dynamics in an identical fashion (Figure 5E). This is despite the connectivity in the network only being moderately sparse (probability of connection is 0.2635). For example, some nodes can display a smaller attractor without mixed mode elements, other nodes contain larger amplitude components while others are essentially still stabilized around their equilibrium point with minimal interference from the rest of the network. Also note that the attractors in Figure 5F occupy a similar region of the reduced phase space (E, I, W^I) as the single and dual node cases when we plot every node $(\boldsymbol{E}_k, \boldsymbol{I}_k, \boldsymbol{W}^I_k)$ in the same reduced phase space.

Given the heterogeneity in the chaotic dynamics of the individual nodes in the coupled networks, we investigated whether node deletion (Figure 5G) or connection deletion (Figure 5H) might enhance the stability of the homeostatic mechanism. Indeed, the homeostatic mechanism is inherently local for a node and trying to stabilize the dynamics of that node despite receiving external, potentially destabilizing inputs. To that end, we deleted a node and recomputed our Hopf bifurcation curves for each node deletion yielding 66 different systems with 65 nodes. In every system, the deletion either had minimal effect on the Hopf-bifurcation curve or it shifted the curve upward. Thus, deleting either connections or nodes can only increase the stability of the homeostatically induced equilibrium. The maximum change was a 14.69% shift upwards (as measured from the peak) given by deleting the 25th node. Deleting individuals connections in the weight matrix, $\boldsymbol{W}^{EE}$ yielded at most a 4.01% shift upwards in the Hopf bifurcation curve. Interestingly, the largest shift in the Hopf-bifurcation curve corresponds to $\boldsymbol{W}^{EE}_{21,4}$ and not node 25. We computed a series of measures of centrality for the nodes that were deleted. These included the row and column sums, authority, hub score, in degree, out degree, page rank, out closeness, in closesness, and betweeness and the reciprocal of the maximum eigenvalue. The reciprocal of the maximum eigenvalue of the weight matrix after node deletion had the largest correlation coefficient with the stability increase (0.999), as expected from our analysis. All other computed metrics displayed weaker correlation coefficients typically falling in the range $0.14 - 0.54$.

6 Discussion

Through a combination of numerical and analytical work, we studied a homeostatically regulated Wilson-Cowan system in three separate cases: isolated single-nodes, reciprocally coupled dual-nodes, and large coupled networks where the connection strength was derived from functional neuroimaging data [Hellyer et al., 2016, Honey et al., 2009, Hagmann et al., 2008]. We found that the isolated single node displays a plethora of complex dynamics such as mixed mode oscillations, chaos via a period-doubling cascade, and mixed-mode chaos. The source of these rich dynamics is a combination of the Hopf-bifurcation induced by the homeostatic mechanism, and the cubic-like critical manifold of the excitatory dynamics. Two nodes with no self coupling and symmetric reciprocal excitatory coupling acted essentially as a single, self-coupled node and synchronized to the steady state attractors in the single node-case. We demonstrated analytically that the stability of steady states in the single node case is directly inherited in the dual node case. Furthermore, any unstable limit cycle in the single node is unstable in the dual node case. Finally, we numerically explored the large coupled network and showed a similar transition to oscillatory behavior for strong enough excitatory coupling. The individual nodes in the large network displayed similar dynamics to isolated recurrently coupled nodes in different parameter regimes. Interestingly, node deletion and connection deletion yielded non-trivial increases in the stability of the homeostatic set point for all values of excitatory to inhibitory coupling.

Past the Hopf-bifurcation, the network exhibits a rich dynamical repertoire consisting of oscillatory activity, chaos, and mixed-mode elements of both. Whether these dynamical states are potentially functional or pathological remains to be seen. Indeed, even for the experimentally determined chaotic attractors in [Babloyantz and Destexhe, 1986], some correspond to functional states such as stages of sleep while others correspond to pathological states such as epileptic seizures. In the former case, we have demonstrated that synaptic homeostasis can support the emergence of complex dynamics. If however, these states are pathological, then they represent a failure of homeostasis in regulating network dynamics. Our node-deletion and connection deletion experiments demonstrate that the deletion of even single nodes or connections can increase the stability of the entire network through a shift in the Hopf-bifurcation curve upwards.

Homeostasis is widely regarded as a mechanism for the maintenance of network dynamics, and more specifically the maintenance of a steady-state average firing rate [Macleod and Zinsmaier, 2006, Frank et al., 2006, Bacci et al., 2001] and is regarded as a stabilizing force in network dynamics [Turrigiano and Nelson, 2004]. This steady-state is regulated at slow time scales on the order of minutes [Frank et al., 2006] or hours [Turrigiano et al., 1998]. For example, the homeostatic model in [Vogels et al., 2011] was shown to maintain the asynchronous irregular regime where neurons fire irregularly, but at a constant average rate. It is thus surprising that low dimensional yet rich structures such as mixed-mode chaotic attractors emerge under the presence of homeostasis.

Our results complement recent work on alternative forms of homeostatic regulation. For example, in [Udeigwe et al., 2017], the authors consider the Bienenstock-Cooper-Monroe (BCM,[Bienenstock et al., 1982]) Rule which also can act as a homeostatic regulator. Here, the authors also find chaos and complex dynamics. In [Zenke et al., 2013], the authors consider a metaplastic tripled-based STDP rule (from [Pfister and Gerstner, 2006]) and derive a mean-field system demonstrating BCM like dynamics. The authors find a critical transition time constant for the stability of the BCM rule. This time constant controls the dynamics of the rate detector of the network. The rule results in runaway potentiation if the time constant is too fast. However, In [Harnack et al., 2015], the authors consider a different homeostatic mechanism not based on the BCM rule but based on intrinsic homeostasis. There, they demonstrate that the time constants for homeostatic control should increase for increased network stability. In all cases, homeostasis can be the source of rich dynamical states and our results corroborate and extend this to inhibitory synaptic homeostasis.

While mixed-mode chaos is an understudied phenomenon, it has been previously documented in the literature [Desroches et al., 2012, Koper, 1995, Krupa et al., 2008, Hauser and Olsen, 1996]. For example, the authors analyze an enzymatic reaction scheme in [Hauser and Olsen, 1996] and demonstrate similar pinched/singular tent-maps for the mixed-mode chaotic attractors they observe. Interestingly, the authors suggest a homoclinic limit cycle as their return mechanism through a version of the classical Shilnikov bifurcation resulting in homoclinic chaos [Kuznetsov, 2013]. Indeed, a Shilnikov bifurcation also appears in other Wilson-Cowan type models with more complicated dynamics in the individual nodes [Van Veen and Liley, 2006].

Our results demonstrate that the rich dynamical states are an intrinsic property of synaptic homeostasis, which is capable of more than stabilizing the average firing rates across a network. With inhibitory synaptic homeostasis, stability can only be guaranteed up to a point in the parameter space. This point is analytically determined and is related to the properties of the tuning curves, the homeostatic set point, and the connectivity between excitatory populations. The resulting dynamics past this point display a rich dynamical repertoire including oscillations and chaos, both of which can occur on two different time scales. This is an intrinsic consequence of the inhibitory synaptic homeostasis rule as the two-dimensional Wilson-Cowan node that we consider is incapable of oscillating without inhibitory synaptic homeostasis. These dynamical repertoires might have functional or pathological consequences for populations of neurons.

Parameter	Numerical Value
a	5
p	0.2
τ_E	1
τ_I	1
τ_W	5
W^E	(see Figure Captions, typically [0,3]
θ	(see Figure Captions, typically [0,10]

Table 1: The parameter values for the system of equations (1)-(3) (single node), (14)-(19) (dual node), and (4)-(6) (full network). Note that for the full network equations, $\boldsymbol{W}^{IE} = \theta \boldsymbol{I}_N$, where $\boldsymbol{I}_N$ is the N dimensional identity matrix, and N consists of the number of nodes.

Figures

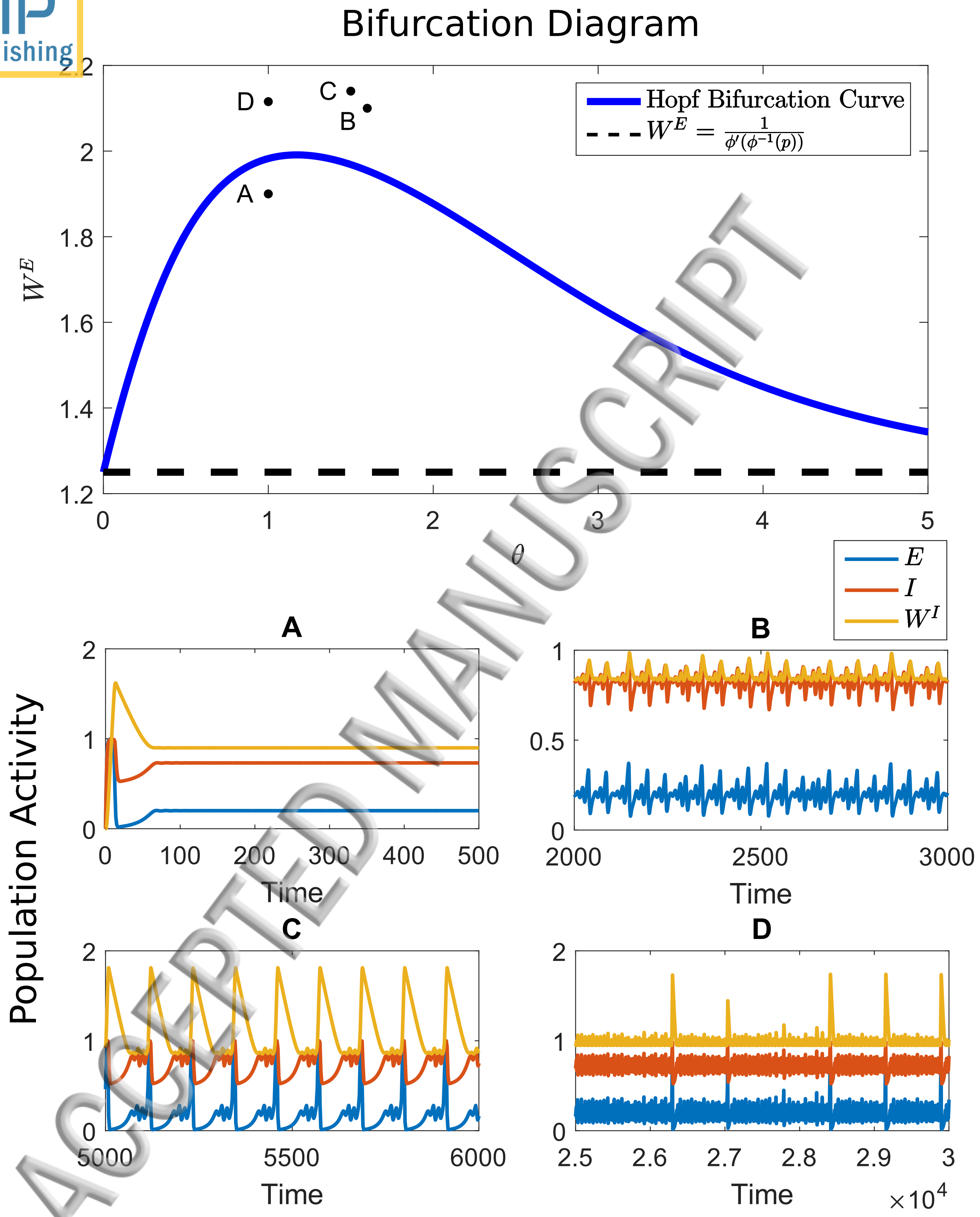
Bifurcation Diagram
Hopf Bifurcation Curve
$W^E = \frac{1}{\phi'(\phi^{-1}(p))}$
W^E
θ
A
B
C
D
2.2
2
1.8
1.6
1.4
1.2
0
1
2
3
4
5
E
I
W^I
Population Activity
Time
0
100
200
300
400
500
0.5
2000
2500
3000
5000
5500
6000
2.5
2.6
2.7
2.8
2.9
3
$\times 10^4$

Figure 1

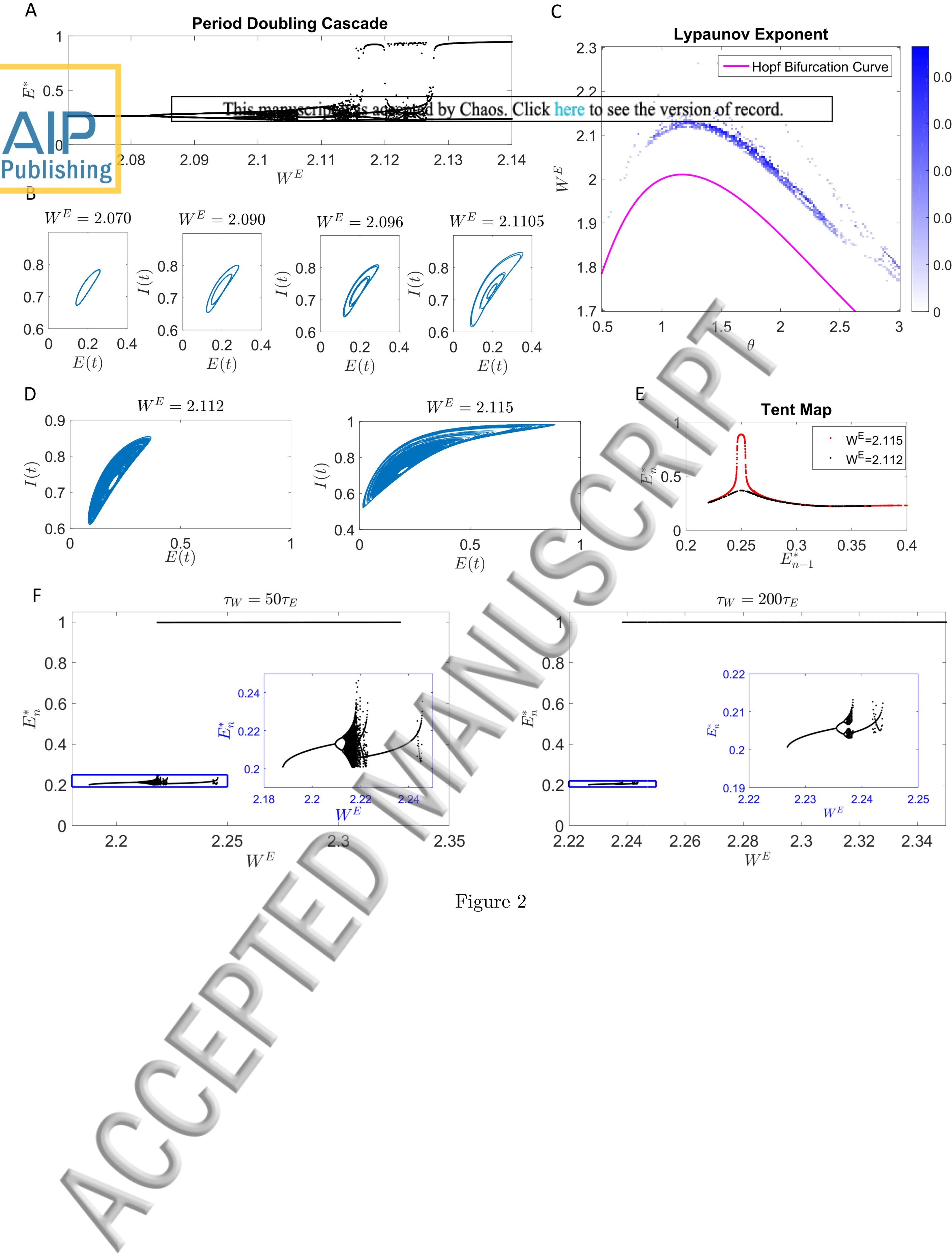
A
Period Doubling Cascade
E^*
1
0.5
0
2.08
2.09
2.1
2.11
2.12
2.13
2.14
W^E
B
$W^E = 2.070$
$W^E = 2.090$
$W^E = 2.096$
$W^E = 2.1105$
$I(t)$
$E(t)$
0.6
0.7
0.8
0
0.2
0.4
C
Lypaunov Exponent
Hopf Bifurcation Curve
W^E
θ
1.7
1.8
1.9
2
2.1
2.2
2.3
0.5
1
1.5
2
2.5
3
0
0.01
0.02
0.03
0.04
0.05
D
$W^E = 2.112$
$W^E = 2.115$
$I(t)$
$E(t)$
0.4
0.6
0.8
0.9
1
0
0.5
1
E
Tent Map
W^E=2.115
W^E=2.112
E^*_n
E^*_{n-1}
0
0.5
1
0.2
0.25
0.3
0.35
0.4
F
$\tau_W = 50\tau_E$
$\tau_W = 200\tau_E$
E^*_n
W^E
0
0.2
0.4
0.6
0.8
1
2.2
2.25
2.3
2.35
2.22
2.24
2.26
2.28
2.3
2.32
2.34
0.2
0.22
0.24
2.18
2.2
2.22
2.24
0.19
0.2
0.21
0.22
2.22
2.23
2.24
2.25

Figure 2

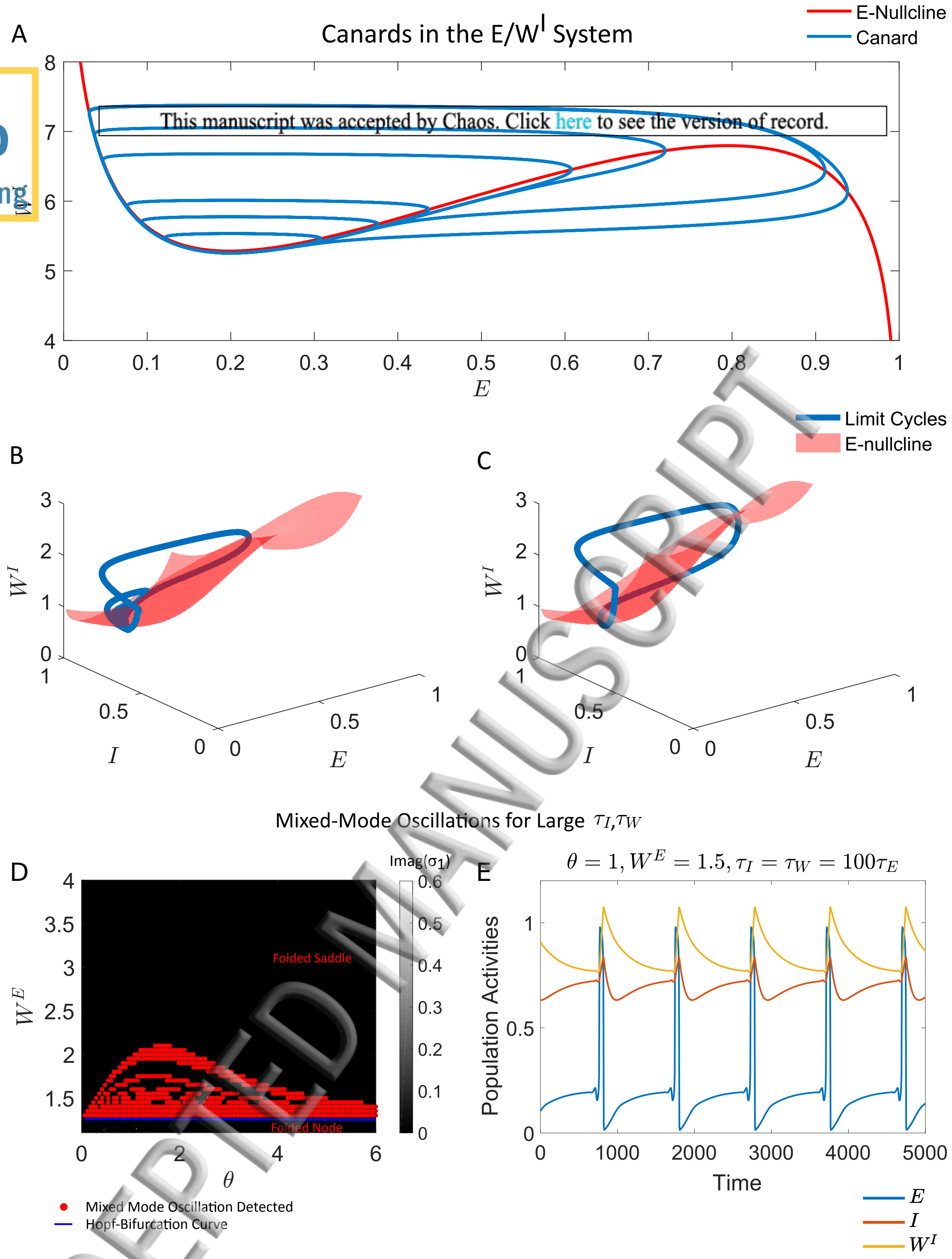
A
Canards in the E/W^I System
E-Nullcline
Canard
W^I
8
7
6
5
4
0
0.1
0.2
0.3
0.4
0.5
0.6
0.7
0.8
0.9
1
E
Limit Cycles
E-nullcline
B
C
W^I
3
2
1
0
1
0.5
0
I
0
0.5
1
E
Mixed-Mode Oscillations for Large τ_I,τ_W
D
W^E
4
3.5
3
2.5
2
1.5
0
2
4
6
θ
Imag(σ_1)
0.6
0.5
0.4
0.3
0.2
0.1
0
Folded Saddle
Folded Node
Mixed Mode Oscillation Detected
Hopf-Bifurcation Curve
E
$\theta = 1, W^E = 1.5, \tau_I = \tau_W = 100\tau_E$
Population Activities
1
0.5
0
0
1000
2000
3000
4000
5000
Time
E
I
W^I

Figure 3

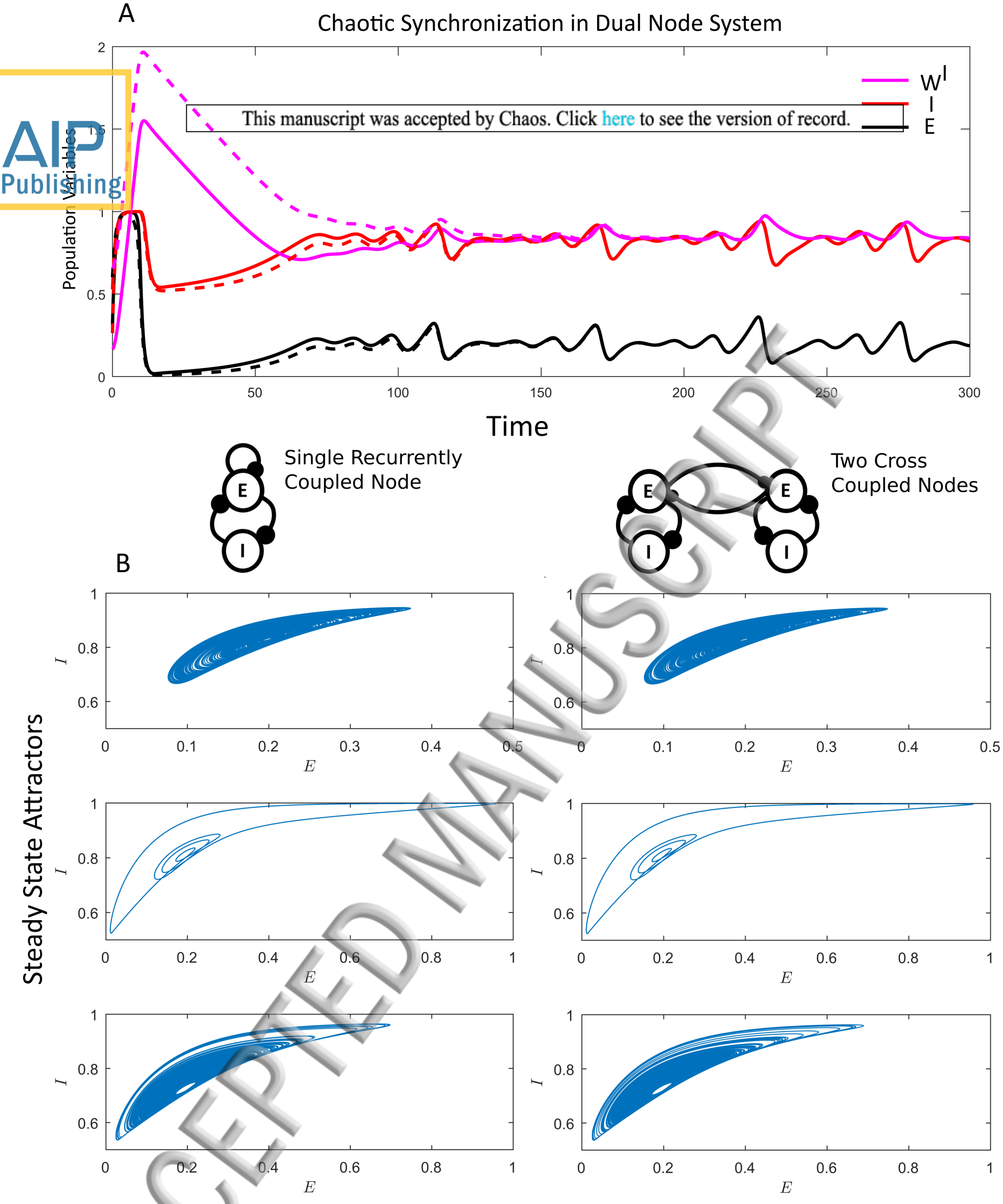
A
Chaotic Synchronization in Dual Node System
Population Variables
2
1.5
1
0.5
0
0
50
100
150
200
250
300
Time
W^I
I
E
Single Recurrently Coupled Node
Two Cross Coupled Nodes
E
I
E
I
E
I
B
Steady State Attractors
I
E
1
0.8
0.6
0
0.1
0.2
0.3
0.4
0.5
0.2
0.4
0.6
0.8
1

Figure 4

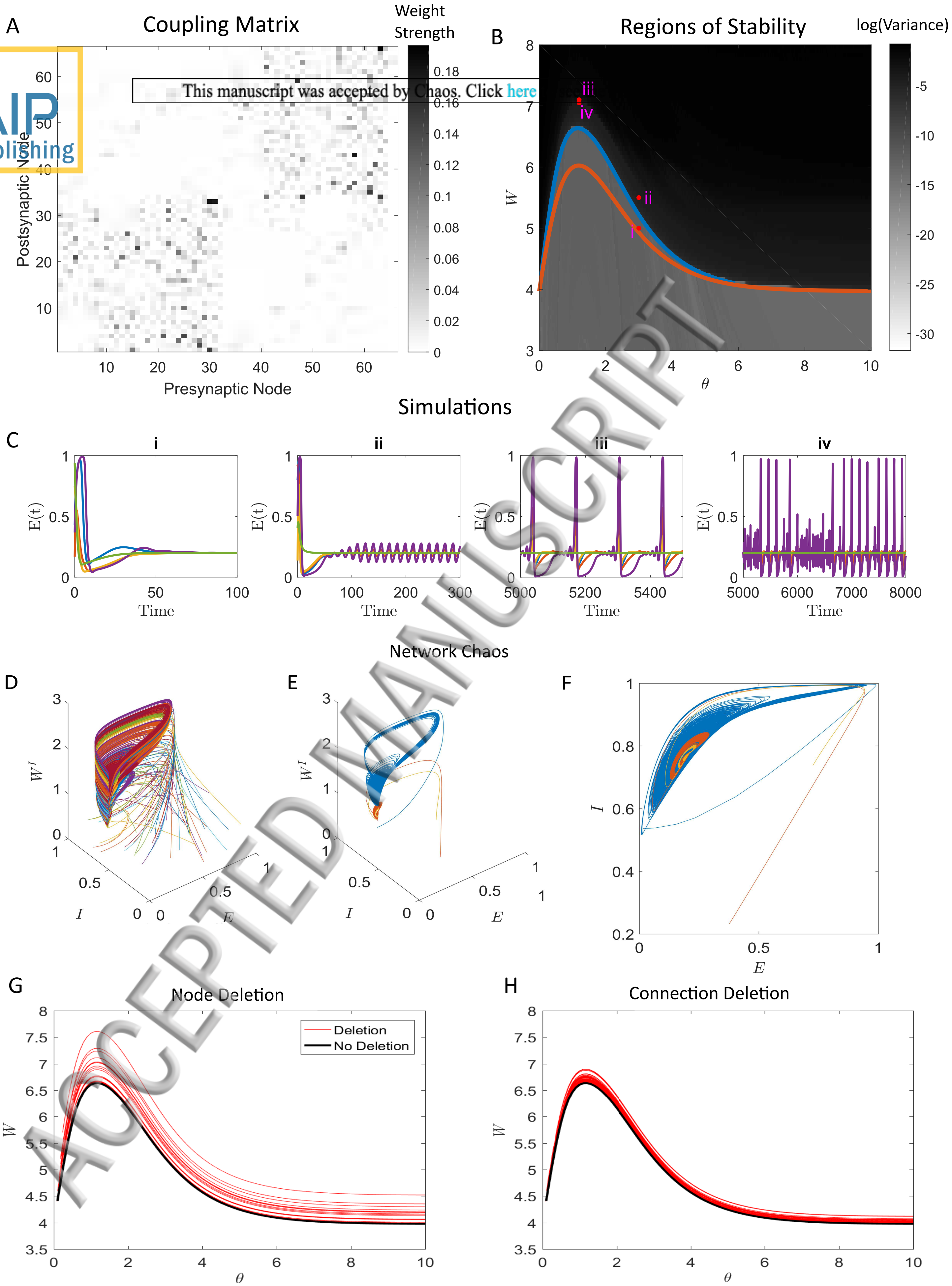
A
Coupling Matrix
Weight Strength
Postsynaptic Node
Presynaptic Node
0.18
0.16
0.14
0.12
0.1
0.08
0.06
0.04
0.02
0
B
Regions of Stability
log(Variance)
W
θ
i
ii
iii
iv
-5
-10
-15
-20
-25
-30
Simulations
C
i
ii
iii
iv
E(t)
Time
Network Chaos
D
E
F
W^I
I
E
G
Node Deletion
Deletion
No Deletion
W
θ
H
Connection Deletion
W
θ

Figure 5

Figure Captions

Figure 1

(Top) The Hopf bifurcation curve for the single-node system can be derived explicitly. Analysis of the $\theta = 0$ case coupled with numerics demonstrates that the bifurcation is a supercritical bifurcation. As we vary the (θ, W^E) parameters, different behaviors emerge corresponding to (A) stability of the target activity, (B) chaotic loss of stability (C) mixed mode oscillations, and (D) mixed mode chaos. The parameters were $p = 0.2$, $\tau_1 = 1$, $\tau_2 = 5$ with (θ, W^E): (1,1.9), (1.6,2.1), (1.5,2.14), (1,2.115) for (A)-(D), respectively. All simulations were conducted in MATLAB using the ode45 integration suite to implement a Runge-Kutta 4th order integration scheme.

Figure 2

(A) The maxima of limit cycles, (E^*) are plotted as a function of the recurrent self coupling, W^E for the single node system. As W^E increases past $W^E_{Hopf}(\theta)$, a period doubling cascade to chaos occurs. (B) The limit cycles and chaotic attractor plotted for increasing values of W^E. (C) The maximum Lyapunov exponent is computed over the two parameter (θ, W^E) region showing patches of chaos that onset after the Hopf bifurcation curve. (D) The chaotic attractor for sub-threshold and mixed mode chaotic solutions. (E) As W^E is increased past $W^E_{Hopf}(\theta)$, the period doubling cascade produces a tent map similar to the classical Lorenz tent map. For larger values of W^E the tent map develops a pseudo-singularity at the maximum value. Note that this is not strictly a singularity in the tent map as the dynamics of the E are restricted to $E \in (0, 1)$. For all simulations in (A),(B),(D) and (E), $\theta = 1$ was used. (F) The mixed-mode oscillations and mixed mode chaos persist for larger separations of relative time scales between the synaptic plasticity (W^I) and the node activities (E, I). On the left, we recompute the limit cycle maxima for $\tau_W = 50\tau_E$, where $\tau_E = 1$ while on the right, we consider $\tau_W = 200\tau_E$. However, mixed-mode solutions are no longer observed for sufficiently large τ_W (not shown). The parameter $\theta = 1.5$ was used for (F).

Figure 3

(A) Canard limit cycles for the dual node system given by equations (24)-(25). The seven limit cycles show a rapid increase in amplitude shortly after a supercritical Hopf bifurcation. The W^E parameter for 6 limit cycles agrees to four decimal places ($W^E = 7.5959$). The final limit cycle is a large relaxation limit cycle ($W^E = 7.6$). The limit cycles were computed with direct simulation of the ordinary differential equations (24)-(25) using a (4,5) order Runge-Kutta scheme. The θ parameter was fixed at $\theta = 1$. (B) Shown above is the period doubled limit cycle (teal) for the system (1)-(3) in addition to the E-nullcline (red). Under the assumption that both the inhibition and the homeostatic mechanism are operating as slow variables, we can see the mixed-mode oscillations potentially arising from the underlying geometry of the folded-node case. The (θ, W^E) parameters were $(2, 2.02)$ (C) A relaxation cycle emerges with increasing values of W^E. For all simulations, $\theta = 1$ was fixed. The (θ, W^E) parameters were $(2.5, 2)$. (D) The folded-singularity conditions were analyzed in the limit that $\tau_I = \tau_W \gg \tau_E$ yielding a continuous folded-node below the Hopf bifurcation curve and a continuous folded saddle region above the Hopf bifurcation curve (See Appendix B for further details)). Mixed mode oscillations were also detected in this limit in the folded-node region. The simulations were automatically classified as mixed-mode oscillations by estimating the variance in their maximum return map of the E variable. Points with high variance correspond to multiple discrete peaks in the return map with larger separation distances in the peaks (and thus mixed-mode solutions) corresponding to larger variance. (E) A simulation of one of the mixed-mode solutions is shown for 5000 time steps, fixed at the values $\theta = 1, W^E = 1.5$ for $\tau_E = 1$, $\tau_W = \tau_I = 200$.

Figure 4

(A) Shown above is the time series for the symmetrically coupled dual node system without self-coupling. The nodes synchronize with each other to a solution state for the single node system at steady-state, independent of where in the parameter region we are or the characteristics of the steady state. The first node is showed in solid lines with the excitation (black), inhibition (red), and homeostatic weight (magenta). The second node is plotted as a dashed line. The parameters in the (W, θ) space are (1.6, 2.1). (B) The steady state attractors for the single node (left) and the dual node (right) are plotted in the (E, I) projection space. The parameters in the (W, θ) are space (1.6,2.1) (top) which corresponds to a chaotic attractor, $(1.5, 2.14)$ (middle) which corresponds to a mixed-mode oscillation, and $(1, 2.115)$ (bottom) which corresponds to mixed-mode chaos. Note that in all cases, the steady state attractors are identical for either the single recurrently coupled node or the dual-node symmetrically coupled nodes. Only one node is plotted in the dual-node case, however due to synchrony, the trajectory for the second node is identical.

Figure 5

(A) The coupling matrix used to connect the excitatory components of the nodes. Note that the matrix is highly structured, and contains no elements on its diagonal (no self-coupling). The system consists of 66 nodes. (B) The Hopf bifurcation (blue) curve is determined manually by evaluating the eigenvalues over the two parameter (θ, W) space numerically and plotting the level set for the first eigenvalue crossing $\mathrm{Re}(\lambda_i) = 0$. This curve was verified by running a mesh of simulations over the (θ, W) parameter space that consisted of 2×10^4 time units each. The final half of the simulation was used to compute the log of the variance of $E_1(t)$ to determine if the equilibrium was stable. Blacker values correspond to either limit cycles or chaos and a loss of stability as the dynamics no longer settle onto a steady state $E_1(t) = p$. Additionally, the analytical approximation (in orange) which assumes that the row-sum of the matrix W^{EE} is approximately constant is also plotted. The accuracy is highest at the asymptotes $(\theta \gg 1, \theta \ll 1)$. The four parameter points (i)-(iv) are shown in (C) in addition to their relationship with the Hopf-Bifurcation curve. The parameter values in the (W, θ) plane are (5,3),(5.5,3),(7.1,1.2), and (7.05,1.2) for (i)-(iv), respectively. Note that the Hopf-bifurcation curve has a similar shape and qualitative behavior to the curve in the single-node/dual-node case. (C) For the parameter values shown, the large network displays a decay to a static equilibrium for $W < W_{Hopf}(\theta)$, stable oscillations for $W > W_{Hopf}(\theta)$, mixed mode oscillations, and mixed-mode chaos. (D) All nodes are plotted in a 3D phase portrait for the parameter region (iv) demonstrating the chaotic attractor. (E) Three nodes are plotted from the full 66-dimensional system in the same phase space. Some nodes in the full system display mixed-mode chaos while simultaneously other nodes display smaller chaotic deviations from the steady state equilibrium. (F) The same figure (E) only projected down to the (E, I) phase space for comparison purposes with Figure 2D. (G) Node deletion (red) and the resulting changes to the numerically Hopf bifurcation curve. The 66 red lines denote deletion of a node, resulting in 66 separate networks containing 65 nodes. (H) As in (G), only single connections are deleted rather than nodes. In total, 1148 non-zero connections exist in the coupling matrix for potential deletion.

References

[Babloyantz and Destexhe, 1986] Babloyantz, A. and Destexhe, A. (1986). Low-dimensional chaos in an instance of epilepsy. *Proceedings of the National Academy of Sciences*, 83(10):3513–3517.

[Bacci et al., 2001] Bacci, A., Coco, S., Pravettoni, E., Schenk, U., Armano, S., Frassoni, C., Verderio, C., De Camilli, P., and Matteoli, M. (2001). Chronic blockade of glutamate receptors enhances presynaptic release and downregulates the interaction between synaptophysin-synaptobrevin–vesicle-associated membrane protein 2. *Journal of Neuroscience*, 21(17):6588–6596.

[Benda and Herz, 2003] Benda, J. and Herz, A. V. (2003). A universal model for spike-frequency adaptation. *Neural computation*, 15(11):2523–2564.

[Bienenstock et al., 1982] Bienenstock, E. L., Cooper, L. N., and Munro, P. W. (1982). Theory for the development of neuron selectivity: orientation specificity and binocular interaction in visual cortex. *Journal of Neuroscience*, 2(1):32–48.

[Brunel, 2000] Brunel, N. (2000). Dynamics of sparsely connected networks of excitatory and inhibitory spiking neurons. *Journal of Computational Neuroscience*, 8(3):183–208.

[Buzsáki, 2002] Buzsáki, G. (2002). Theta oscillations in the hippocampus. *Neuron*, 33(3):325–340.

[Buzsáki et al., 2012] Buzsáki, G., Anastassiou, C. A., and Koch, C. (2012). The origin of extracellular fields and currents—eeg, ecog, lfp and spikes. *Nature Reviews Neuroscience*, 13(6):407–420.

[Buzsáki and Wang, 2012] Buzsáki, G. and Wang, X.-J. (2012). Mechanisms of gamma oscillations. *Annual Review of Neuroscience*, 35:203–225.

[Churchland et al., 2012] Churchland, M. M., Cunningham, J. P., Kaufman, M. T., Foster, J. D., Nuyujukian, P., Ryu, S. I., and Shenoy, K. V. (2012). Neural population dynamics during reaching. *Nature*, 487(7405):51–56.

[Coombes et al., 2018] Coombes, S., Lai, Y. M., ŞAYLI, M., and Thul, R. (2018). Networks of piecewise linear neural mass models. *European Journal of Applied Mathematics*, pages 1–22.

[Desroches et al., 2012] Desroches, M., Guckenheimer, J., Krauskopf, B., Kuehn, C., Osinga, H. M., and Wechselberger, M. (2012). Mixed-mode oscillations with multiple time scales. *SIAM Review*, 54(2):211–288.

[Frank et al., 2006] Frank, C. A., Kennedy, M. J., Goold, C. P., Marek, K. W., and Davis, G. W. (2006). Mechanisms underlying the rapid induction and sustained expression of synaptic homeostasis. *Neuron*, 52(4):663–677.

[Froemke et al., 2007] Froemke, R. C., Merzenich, M. M., and Schreiner, C. E. (2007). A synaptic memory trace for cortical receptive field plasticity. *Nature*, 450(7168):425–429.

[Guckenheimer and Holmes, 2013] Guckenheimer, J. and Holmes, P. (2013). *Nonlinear oscillations, dynamical systems, and bifurcations of vector fields*, volume 42. Springer Science & Business Media.

[Hagmann et al., 2008] Hagmann, P., Cammoun, L., Gigandet, X., Meuli, R., Honey, C. J., Wedeen, V. J., and Sporns, O. (2008). Mapping the structural core of human cerebral cortex. *PLoS biology*, 6(7):e159.

[Harnack et al., 2015] Harnack, D., Pelko, M., Chaillet, A., Chitour, Y., and van Rossum, M. C. (2015). Stability of neuronal networks with homeostatic regulation. *PLoS Computational Biology*, 11(7):e1004357.

[Harris and Ermentrout, 2015] Harris, J. and Ermentrout, B. (2015). Bifurcations in the wilson–cowan equations with nonsmooth firing rate. *SIAM Journal on Applied Dynamical Systems*, 14(1):43–72.

[Hauser and Olsen, 1996] Hauser, M. J. and Olsen, L. F. (1996). Mixed-mode oscillations and homoclinic chaos in an enzyme reaction. *Journal of the Chemical Society, Faraday Transactions*, 92(16):2857–2863.

[Hellyer et al., 2016] Hellyer, P. J., Jachs, B., Clopath, C., and Leech, R. (2016). Local inhibitory plasticity tunes macroscopic brain dynamics and allows the emergence of functional brain networks. *NeuroImage*, 124:85–95.

[Honey et al., 2009] Honey, C., Sporns, O., Cammoun, L., Gigandet, X., Thiran, J.-P., Meuli, R., and Hagmann, P. (2009). Predicting human resting-state functional connectivity from structural connectivity. *Proceedings of the National Academy of Sciences*, 106(6):2035–2040.

[Koper, 1995] Koper, M. T. (1995). Bifurcations of mixed-mode oscillations in a three-variable autonomous van der pol-duffing model with a cross-shaped phase diagram. *Physica D: Nonlinear Phenomena*, 80(1-2):72–94.

[Krupa et al., 2008] Krupa, M., Popović, N., and Kopell, N. (2008). Mixed-mode oscillations in three time-scale systems: a prototypical example. *SIAM Journal on Applied Dynamical Systems*, 7(2):361–420.

[Krupa and Szmolyan, 2001] Krupa, M. and Szmolyan, P. (2001). Relaxation oscillation and canard explosion. *Journal of Differential Equations*, 174(2):312–368.

[Krupa and Wechselberger, 2010] Krupa, M. and Wechselberger, M. (2010). Local analysis near a folded saddle-node singularity. *Journal of Differential Equations*, 248(12):2841–2888.

[Kuznetsov, 2013] Kuznetsov, Y. A. (2013). *Elements of applied bifurcation theory*, volume 112. Springer Science & Business Media.

[Litwin-Kumar and Doiron, 2012] Litwin-Kumar, A. and Doiron, B. (2012). Slow dynamics and high variability in balanced cortical networks with clustered connections. *Nature Neuroscience*, 15(11):1498.

[Lorenz, 1963] Lorenz, E. N. (1963). Deterministic nonperiodic flow. *Journal of the Atmospheric Sciences*, 20(2):130–141.

[Macleod and Zinsmaier, 2006] Macleod, G. T. and Zinsmaier, K. E. (2006). Synaptic homeostasis on the fast track. *Neuron*, 52(4):569–571.

[Markram and Tsodyks, 1996] Markram, H. and Tsodyks, M. (1996). Redistribution of synaptic efficacy between neocortical pyramidal neurons. *Nature*, 382(6594):807.

[Nicola and Campbell, 2016] Nicola, W. and Campbell, S. A. (2016). Nonsmooth bifurcations of mean field systems of two-dimensional integrate and fire neurons. *SIAM Journal on Applied Dynamical Systems*, 15(1):391–439.

[Pecora and Carroll, 1990] Pecora, L. M. and Carroll, T. L. (1990). Synchronization in chaotic systems. *Physical review letters*, 64(8):821.

[Pfister and Gerstner, 2006] Pfister, J.-P. and Gerstner, W. (2006). Triplets of spikes in a model of spike timing-dependent plasticity. *Journal of Neuroscience*, 26(38):9673–9682.

[Sprott and Sprott, 2003] Sprott, J. C. and Sprott, J. C. (2003). *Chaos and time-series analysis*, volume 69. Oxford University Press Oxford.

[Stevens and Wang, 1995] Stevens, C. F. and Wang, Y. (1995). Facilitation and depression at single central synapses. *Neuron*, 14(4):795–802.

[Strogatz, 2014] Strogatz, S. H. (2014). *Nonlinear dynamics and chaos: with applications to physics, biology, chemistry, and engineering*. Hachette UK.

[Turrigiano et al., 1998] Turrigiano, G. G., Leslie, K. R., Desai, N. S., Rutherford, L. C., and Nelson, S. B. (1998). Activity-dependent scaling of quantal amplitude in neocortical neurons. *Nature*, 391(6670):892–896.

[Turrigiano and Nelson, 2004] Turrigiano, G. G. and Nelson, S. B. (2004). Homeostatic plasticity in the developing nervous system. *Nature Reviews Neuroscience*, 5(2):97–107.

[Udeigwe et al., 2017] Udeigwe, L. C., Munro, P. W., and Ermentrout, G. B. (2017). Emergent dynamical properties of the bcm learning rule. *The Journal of Mathematical Neuroscience*, 7(1):2.

[Van Veen and Liley, 2006] Van Veen, L. and Liley, D. T. (2006). Chaos via shilnikov's saddle-node bifurcation in a theory of the electroencephalogram. *Physical Review Letters*, 97(20):208101.

[Vo and Wechselberger, 2015] Vo, T. and Wechselberger, M. (2015). Canards of folded saddle-node type i. *SIAM Journal on Mathematical Analysis*, 47(4):3235–3283.

[Vogels et al., 2011] Vogels, T. P., Sprekeler, H., Zenke, F., Clopath, C., and Gerstner, W. (2011). Inhibitory plasticity balances excitation and inhibition in sensory pathways and memory networks. *Science*, 334(6062):1569–1573.

[Wechselberger, 2005] Wechselberger, M. (2005). Existence and bifurcation of canards in $\mathbb{R}^3$ in the case of a folded node. *SIAM Journal on Applied Dynamical Systems*, 4(1):101–139.

[Wiggins, 2003] Wiggins, S. (2003). *Introduction to applied nonlinear dynamical systems and chaos*, volume 2. Springer Science & Business Media.

[Wilson and Cowan, 1972] Wilson, H. R. and Cowan, J. D. (1972). Excitatory and inhibitory interactions in localized populations of model neurons. *Biophysical Journal*, 12(1):1–24.

[Zenke et al., 2013] Zenke, F., Hennequin, G., and Gerstner, W. (2013). Synaptic plasticity in neural networks needs homeostasis with a fast rate detector. *PLoS Computational Biology*, 9(11):e1003330.

Appendices

Appendix A: First Lyapunov Coefficient for the $\theta = 0$ Case

We can compute the Lyapunov coefficient for the Hopf bifurcation point when $\theta = 0$ quite easily without having to resort to the center-manifold theorem. By setting $\theta = 0$, we have the following system

$$\begin{aligned} \tau_1 E' &= -E + \phi\left(W^E E - W^I I\right) \\ I' &= -I + \phi(0) \\ \tau_2 W^{I'} &= I(E - p) \end{aligned}$$

and in essence $I(t)$ has become decoupled from the other equations and can be set to its equilibrium value of $\phi(0)$. This reduction yields

$$\begin{aligned} \tau_1 E' &= -E + \phi\left(W^E E - W^I\right) \\ \tau_2 W^{I'} &= (E - p) \end{aligned}$$

after rescaling τ_2 and W^I to absorb $I = \phi(0)$. To proceed, we shift the equilibrium to the origin

$$\begin{aligned} \hat{E} &= E - p \\ \hat{W} &= W^I - W^E p + \phi^{-1}(p) \end{aligned}$$

which yields the following

$$\begin{aligned} \tau_1 \hat{E}' &= -\hat{E} - p + \phi(W^E(p + \hat{E}) - (\hat{W} + W^E p - \phi^{-1}(p)) \\ &= -\hat{E}(1 - W^E \phi'(\phi^{-1}(p))) - \phi'(\phi^{-1}(p))\hat{W} + \frac{\phi''(\phi^{-1}(p))}{2!}[W^E\hat{E} - \hat{W}]^2 \\ &+ \frac{\phi'''(\phi^{-1}(p))}{3!}[W^E\hat{E} - \hat{W}]^3 + O((W^E\hat{E} - \hat{W})^4) \\ \tau_2 \hat{W}' &= \hat{E} \end{aligned}$$

If we now apply the bifurcation condition:

$$W^E = \phi'(\phi^{-1}(p))^{-1} = \frac{1}{ap(1-p)}$$

we obtain the following system

$$\begin{aligned} \tau_1 \hat{E}' &= -ap(1-p))\hat{W} + \frac{\phi''(\phi^{-1}(p))}{2!}[W^E\hat{E} - \hat{W}]^2 + \frac{\phi'''(\phi^{-1}(p))}{3!}[W^E\hat{E} - \hat{W}]^3 \\ &+ O((W^E\hat{E} - \hat{W})^4) \\ \hat{W}' &= \frac{\hat{E}}{\tau_2} \end{aligned}$$

This system can be transformed with $\hat{E} = K\tilde{E}$ into a system of the form

$$\begin{aligned} \tilde{E}' &= -\omega\hat{W} + \frac{\phi''(\phi^{-1}(p))}{2!K\tau_1}[W^E K\tilde{E} - \hat{W}]^2 + \frac{\phi'''(\phi^{-1}(p))}{3!K\tau_1}[W^E K\tilde{E} - \hat{W}]^3 + O((W^E K\tilde{E} - \hat{W})^4) \\ &= -\omega\hat{W} + P(\tilde{E}, \hat{W}) \\ \hat{W}' &= \omega\tilde{E} \end{aligned}$$

where

$$K = \sqrt{\frac{\tau_2 ap(1-p)}{\tau_1}}, \quad \omega = \sqrt{\frac{ap(1-p)}{\tau_2\tau_1}}$$

which is the standard form to compute the Lyapunov Coefficient for a two-dimensional function. The formula for the Lypaunov coefficient can be found in [Guckenheimer and Holmes, 2013] The resulting computation yields

$$l_1(0) = \frac{W^E_{Hopf}((KW^E_{Hopf})^2 + 1)}{16\tau_1}\left(\phi'''(\phi^{-1}(p)) - \frac{\phi''(\phi^{-1}(p))^2}{K\omega\tau_1}\right)$$

which for the sigmoid we consider simplifies to:

$$l_1(0) = -\frac{W^E_{Hopf}((KW^E_{Hopf})^2 + 1)}{16\tau_1}\left(a^3p^2(1 - p^2)\right) < 0$$

and thus the bifurcation is supercritical, always.

Appendix B: Canards and Mixed Mode Oscillatons: Potential Sources of Origin

Existence of Canards in the 2D (E, W^I) System

Here, we will conisder the emergence of Canards in the two-dimensional system:

$$\begin{aligned} E' &= -E + \phi(W^E E - W^I) && (36)\\ W^{I\prime} &= \epsilon(E - p) && (37) \end{aligned}$$

which arises in the small θ limit as I decays to its steady state $\phi(0) = \frac{1}{2}$ independent of all other dynamics, and upon suitably redefining the both time and space variables to absorb the $\phi(0)$ term into W^I and τ_W. Here, we will prove the existence of Canard solutions through the determination of a Canard point (see [Krupa and Szmolyan, 2001] for further details). For the fast-slow system given by

$$\begin{aligned} \dot{x} &= f(x, y, \lambda, \epsilon)\\ \dot{y} &= \epsilon g(x, y, \lambda, \epsilon) \end{aligned}$$

a series of conditions ([Krupa and Szmolyan, 2001]) have to be satisfied to guarantee the existence of Canards which we include here for convenience:

1. The critical manifold, given by $f(x, y, \lambda, 0)$ is s-shaped, with one critical point at the origin corresponding to a minimum. It can be written in the form $y = \psi(x)$

2. Consider the following branches:

$$\begin{aligned} S_L &= \{(x, \psi(x)) : x < 0\}\\ S_M &= \{(x, \psi(x)) : 0 < x < x_M\}\\ S_R &= \{(x, \psi(x)) : x > x_M\} \end{aligned}$$

   where X_M corresponds to the maximum critical point. Then, S_L and S_R are attracting ($\frac{\partial f}{\partial x} < 0$) while S_M is repelling ($\frac{\partial f}{\partial x} > 0$) for the layer problem.

3. One of the folds becomes a Canard point, $g(0, 0, 0, 0) = 0$ while the other fold is non-degenerate. The canard point is genertic if the following also hold:

$$\frac{\partial^2 f}{\partial x^2}(0, 0, 0, 0) \neq 0, \quad \frac{\partial f}{\partial y}(0, 0, 0, 0) \neq 0, \quad \frac{\partial g}{\partial x}(0, 0, 0, 0) \neq 0, \quad \frac{\partial g}{\partial \lambda}(0, 0, 0, 0) \neq 0$$

4. When $\lambda = 0$, then $\dot{x} < 0$ on S_R and and $\dot{x} > 0$ on $S_L \cup \{0\} \cup S_M$. This specifically concerns the flow on the critical manifold, given by:

$$\dot{x} = \frac{g(x, \psi(x), 0)}{\psi'(x)}$$

These are necessary conditions required for the Canard point to exist, and be generic. Here, we will limit our analysis to the sigmoid given by (10) for simplicity. The critical manifold is given by

$$\begin{aligned} W^I &= \psi(E) = W^E E - \phi^{-1}(E)\\ \psi'(E) &= W^E - \frac{d\phi^{-1}(E)}{dE}\\ &= W^E - \frac{1}{aE(1 - E)} \end{aligned}$$

which yields the following two potential folds:

$$E(1-E)-(W^Ea)^{-1}=0$$
$$E=\frac{1}{2}\pm\sqrt{\frac{1}{4}-\frac{1}{aW^E}}$$

The criticality of these points is given by $\psi''(E)$:

$$\begin{aligned}
\psi''(E) &= -(-1)\left(\phi'(\phi^{-1}(E))\right)^{-2}\phi''(\phi^{-1}(E))\frac{d\phi^{-1}(E)}{dE}\\
&= \frac{a^2\phi(\phi^{-1}(E))(1-\phi(\phi^{-1}(E)))(1-2\phi(\phi^{-1}(E)))}{a^3\phi(\phi^{-1}(E))^3(1-\phi(\phi^{-1}(E)))^3}\\
&= \frac{(1-2E)}{(aE(1-E))^2}\\
\psi''(E_\pm) &= (W^E)^2(1-2E_\pm)=(W^E)^2\left(\mp\sqrt{\frac{1}{4}-\frac{1}{aW^E}}\right)
\end{aligned}$$

which yields $\psi''(E_-)>0$ and $\psi''(E_+)<0$. This, E_- is a minimum while E_+ is a maximum, and condition 1 is satisfied. Condition 2 concerns equilibria of the layer problem. Specifically, if we regard W^I as a fixed parameter, then:

$$\begin{aligned}
E' &= -E+\phi(W^EE-W^I)=f(E,W^I)\\
\frac{\partial f}{\partial E} &= -1+W^E\phi'(W^EE-W^I)=-1+W^Ea\phi(W^EE-W^I)(1-\phi(W^EE-W^I))\\
&= -1+W^EaE(1-E)\\
\frac{\partial f}{\partial E} &= -W^Ea(E-E_-)(E-E_+)
\end{aligned}$$

which given that $E_-<E_+$, implies that for $E<E_-$ and for $E>E_+$, $\frac{\partial f}{\partial E}<0$ while for $E_-<E<E_+$, $\frac{\partial f}{\partial E}>0$ and condition 2 is satisfied. The primary Canard condition is that one of the fold points becomes a Canard point, ie. it coincides with an equilibrium of the slow system: $g(E_\pm,\psi(E_\pm),0,0)=0$. The Canard condition yields the following potential Canard points:

$$E\pm=p\to p=\frac{1}{2}\pm\sqrt{\frac{1}{4}-\frac{1}{aW^E}}$$

Further, the conditions $\frac{\partial g}{\partial E}\neq 0$ and $\frac{\partial g}{\partial p}\neq 0$ are satisfied always. The next condition involves the second partial of f, evaluated at $E_\pm$, and $W^I_\pm=W^EE_\pm-\phi^{-1}(E_\pm)$:

$$\begin{aligned}
\frac{\partial^2 f}{\partial E^2} &= (aW^E)^2\phi(W^EE-W^I)(1-\phi(W^EE-W^I))(1-2\phi(W^EE-W^I))\\
&= (aW^E)^2\phi(\phi^{-1}(E_\pm))(1-\phi(\phi^{-1}(E_\pm)))(1-2\phi(\phi^{-1}(E_\pm)))\\
&= (aW^E)^2E_\pm(1-E_\pm)(1-2E_\pm)\\
&= aW^E(1-2E_\pm)=aW^E\left(\pm 2\sqrt{\frac{1}{4}-\frac{1}{aW^E}}\right)
\end{aligned}$$

which implies that we require $aW^E\neq\frac{1}{4}$.

The next condition is that $\frac{\partial f}{\partial W^I}\neq 0$

$$\frac{\partial f}{\partial W^I}=-\phi'(W^EE-W^I)$$
$$\begin{aligned}
&= -a\phi(W^EE-W^I)(1-\phi(W^EE-W^I)\\
&= -a\phi(\phi^{-1}(E_\pm))(1-\phi^{-1}(E_\pm)\\
&= -aE_\pm(1-E_\pm)\\
&= -W^{E^{-1}}
\end{aligned}$$

which implies we only need W^E to be bounded, or non-zero if the non-genericity condition is based on taking a coordinate transform. Now, for the final condition, we have to consider the reduced flow with the $\lambda = 0$ condition being $p = E_\pm$:

$$\begin{aligned}\dot{E}_\pm &= \frac{E - E_\pm}{W^E - \frac{1}{aE(1-E)}} = \frac{E(1-E)(E-E_\pm)}{W^E(E(E-1)-(aW^E)^{-1})}\\ &= -\frac{E(1-E)(E-E_\pm)}{W^E(E-E_+)(E-E_-))}\end{aligned}$$

We'll consider the $p = E_-$ case:

$$\dot{E}_- = -\frac{E(1-E)}{W^E(E-E_+)}$$

First, note that $0 < E < E_- < E_+$. This implies that for $0 < E < E_-$, $\dot{E} > 0$. Further, for $E_- < E < E_+$, $\dot{E}_- > 0$, as neither the numerator nor denominanator change sine. Further, $\dot{E}_\pm > 0$ for $E = E_-$. To proceed further, we will need to transform the system into the following form:

$$\begin{aligned}x' &= -yh_1(x,y,\lambda,\epsilon) + x^2h_2(x,y,\lambda,\epsilon) + \epsilon h_3(x,y,\lambda,\epsilon)\\ y' &= \epsilon(xh_3(x,y,\lambda,\epsilon) - \lambda h_5(x,y,\lambda,\epsilon) + yh_6(x,y,\lambda,\epsilon))\end{aligned}$$

First, consider the transform:

$$\begin{aligned}\hat{E} &= E - E_-\\ \hat{W}^I &= W^I - W^I_- = W^I - W^E E_- + \phi^{-1}(E_-)\\ \hat{p} &= p - E_-\end{aligned}$$

to shift all variables to the origin. This yields the following:

$$\begin{aligned}\hat{E}' &= -\hat{E} - E_- + \phi\left(W^E\hat{E} - \hat{W}^I + \phi^{-1}(E_-)\right)\\ \hat{W}^{I\prime} &= \epsilon(\hat{E} - \hat{p})\end{aligned}$$

Further, to transform the system into canonical form, we use:

$$\begin{aligned}\hat{Z} &= W^E\hat{E} - \hat{W}^I\\ \hat{W}^I &= \hat{W}^I\end{aligned}$$

which yields the following:

$$\begin{aligned}\hat{Z}' &= -\hat{W}^I + \hat{Z}^2\left(W^E\frac{\phi''(\phi^{-1}(E_-))}{2!} + W^E\hat{Z}\frac{\phi'''(\phi^{-1}(E))}{3!} + O(\hat{Z}^2)\right) + \epsilon\left(\frac{\hat{Z}+\hat{W}^I}{W^E} - \hat{p}\right)\\ \hat{W}^{I\prime} &= \epsilon\left(\frac{\hat{Z}+\hat{W}^I}{W^E} - \hat{p}\right)\\ &= \epsilon\left(\frac{\hat{Z}}{W^E} - \hat{p} + \frac{\hat{W}^I}{W^E}\right)\end{aligned}$$

In order to apply the theorems from [Krupa and Szmolyan, 2001], we require another round of transforms to put the system into proper canonical form. Consider the transform $x = \hat{Z}M$ and $y = \hat{W}^I N$

$$\begin{aligned}x' &= -\frac{My}{N} + \frac{x^2}{M}\left(W^E\frac{\phi''(\phi^{-1}(E_-))}{2!} + W^E\frac{x}{M}\frac{\phi'''(\phi^{-1}(E))}{3!} + O(x^2)\right) + \tilde{\epsilon}\left(x + \frac{My}{N} - W^E M\hat{p}\right)\\ y' &= \tilde{\epsilon}\left(\frac{Nx}{M} - (W^E N\hat{p}) + y\right) \quad (\text{where} \quad \tilde{\epsilon} = \epsilon(W^E)^{-1})\end{aligned}$$

which yields the following functions:

$$\begin{aligned}
h_1(x,y,\lambda,\tilde{\epsilon}) &= \frac{M}{N} \\
h_2(x,y,\lambda,\tilde{\epsilon}) &= W^E\frac{\phi''(\phi^{-1}(E_-))}{M2!} + W^E\frac{x}{M^2}\frac{\phi'''(\phi^{-1}(E))}{3!} + O(x^2) \\
h_3(x,y,\lambda,\tilde{\epsilon}) &= \left(x + \frac{My}{N} - W^E M\hat{p}\right) \\
h_4(x,y,\lambda,\tilde{\epsilon}) &= \frac{N}{M} \\
h_5(x,y,\lambda,\tilde{\epsilon}) &= W^E N \\
h_6(x,y,\lambda,\tilde{\epsilon}) &= 1
\end{aligned}$$

If we take $N = M = \left(W^E\frac{\phi''(\phi^{-1}(E_-))}{2!}\right)$, and absorb $W^E M$ into $\hat{p}$ with $\lambda = W^E M\hat{p}$, we are in the correct normal form and arrive at the following:

$$\begin{aligned}
a_1 &= \frac{\partial h_3(0,0,0,0)}{\partial x} = 1 \\
a_2 &= \frac{\partial h_1(0,0,0,0)}{\partial x} = 0 \\
a_3 &= \frac{\partial h_2(0,0,0,0)}{\partial x} = \frac{2!2!\phi'''(\phi^{-1}(E))}{W^E 3!\phi''(\phi^{-1}(E_-))^2} \\
a_4 &= \frac{\partial h_4(0,0,0,0)}{\partial x} = 0 \\
a_5 &= h_6(0,0,0,0) = 1
\end{aligned}$$

Then consider the quantity:

$$\begin{aligned}
A &= -a_2 + 3a_3 - 2a_4 - 2a_5 \\
&= -4\left(\frac{E_-(1-E_-)}{(1-2E_-)^2}\right) = -\frac{4}{aW^E(1-2E_-)^2} < 0
\end{aligned}$$

Thus, $A < 0$ which implies that the Hopf bifurcation that coincides with the Canard point is a super-critical generic Hopf bifurcation (as also demonstrated by our Lypaunov coefficient analysis). Further, the Hopf-bifurcation vanishes to leading order (in fact all orders, see above) as for $\epsilon > 0$, the Hopf point occurs when

$$\lambda_H(\tilde{\epsilon}) = -\left(\frac{a_1 + a_5}{2}\right)\tilde{\epsilon} + O(\epsilon^{3/2}) = -\epsilon + O(\epsilon^{3/2})$$

which we will now express in the original parameter system:

$$\begin{aligned}
\lambda_H(\epsilon) = -\frac{\epsilon}{W^E} + O(\epsilon^{3/2}) &= W^E N\hat{p} \\
&= \frac{(W^E)^2\phi''(\phi^{-1}(E_-))}{2!}(p - E_-) \\
&= \frac{(W^E)^2\phi''(\phi^{-1}(E_-))}{2!}(p - E_-) \\
-\frac{\epsilon}{W^E} + O(\epsilon^{3/2}) &= \frac{(W^E)^2\phi''(\phi^{-1}(E_-))}{2!}\left(p - \frac{1}{2} + \sqrt{\frac{1}{4} - \frac{1}{aW^E}}\right)
\end{aligned}$$

Note that if we expand out $W^E(\epsilon)$, then the $O(1)$ problem yields the following

$$W^E = \frac{1}{ap(1-p)}$$

which is identical to the equation we derived before.

Folded-Node Analysis for $\tau_I \gg \tau_E$, $\tau_W \gg \tau_E$, $\tau_I = \tau_W$

Here, we will consider the 3D system:

$$\begin{aligned} \epsilon E' &= -E + \phi(W^E E - W^I I) = f(E, I, W^I) \\ I' &= -I + \phi(\theta E) = g_1(E, I, W^I) \\ W^I &= I(E-p) = g_2(E, I, W^I) \end{aligned}$$

where we have absorbed the excitatory time-constant and assumed that I and W^I are two slow variables. First, from the analysis in [Desroches et al., 2012, Wechselberger, 2005] we have the following set of genericity conditions:

$$\begin{aligned} f(p^*, 0) &= 0 \\ \frac{\partial f(p^*, 0)}{\partial E} &= 0 \\ \frac{\partial^2 f(p^*, 0)}{\partial E^2} &\neq 0 \\ D_{(I, W^I)} f(p^*, 0) & \quad \text{has full rank one} \end{aligned}$$

The first condition yields:

$$E = \phi(W^E E - W^I I)$$

while the second condition yields:

$$\begin{aligned} -1 + W^E \phi'(W^E E - W^I I) &= -1 + W^E a\phi(W^E E - W^I I)(1 - \phi(W^E E - W^I I)) \\ &= -1 + W^E aE(1-E) = 0 \end{aligned}$$

which again yields $E_\pm$ as in the 2D, Canard case. The third condition yields:

$$\begin{aligned} -(W^E)^2 \phi''(W^E E - W^I) &= -(W^E)^2 a\phi(W^E E - W^I)(1 - \phi(W^E E - W^I))(1 - 2\phi(W^E E - W^I I)) \\ &= -(W^E)^2 aE_-(1 - E_-)(1 - 2E_-) \\ &= -W^E(1 - 2E_-) \neq 0 \end{aligned}$$

where the last step is verified from our analysis in the 2D case. Finally, the last condition yields

$$\begin{aligned} D_{y,z} f &= [-W^I \phi'(W^E E - W^I), -I\phi'(W^E E - W^I)] \\ &= \left[-\frac{W^I}{W^E}, -\frac{I}{W^E}\right] \end{aligned}$$

which is always full rank. Now we need to consider the dynamics restricted to the critical manifold:

$$\begin{aligned} \dot{E} &= \frac{\partial f}{\partial I} g_1 + \frac{\partial f}{\partial W^I} g_2 = -(-I + \phi(\theta E)) W^I \phi'(W^E E - W^I I) - I^2(E-p)\phi'(W^E E - W^I I) \\ \dot{I} &= -\frac{\partial f}{\partial E} g_1 = (-1 + W^E \phi'(W^E E - W^I I))(-I + \phi(\theta E)) \\ \dot{W^I} &= -\frac{\partial f}{\partial E} g_2 = (-1 + W^E \phi'(W^E E - W^I I))(I(E-p)) \end{aligned}$$

and the fold-point becomes a folded singularity if:

$$\begin{aligned} \frac{\partial f}{\partial I} g_1 + \frac{\partial f}{\partial W^I} g_2 &= -\left(-I + \phi(\theta E)\right) W^I \phi'(W^E E - W^I) - \left(I^2(E-p)\right) \phi'(W^E E - W^I) = 0 \\ &\rightarrow -\left(-I + \phi(\theta E_-)\right) W^I - \left(I^2(E-p)\right) = 0 \end{aligned}$$

which yields a fold point when:

$$W^I = \frac{-I^2(E_- - p)}{-I + \phi(\theta E_-)}$$

Thus, the fold point is determined by the following equations:

$$E = E_-, \quad W^I = \frac{-I^2(E_- - p)}{-I + \phi(\theta E_-)} = \omega(I, E_-)$$

with I_- being determined by:

$$-E_- + \phi(W^E E_- - \omega(I, E_-)I) = 0 \tag{38}$$

As the following computations are quite tedious, we employed a computer algebra system (Maple) to resolve them. We will consider the fold point as (E_-, I_-, W^I_-). Evaluating the Jacobian yields the following:

$$J = \begin{pmatrix} -W^I_- \frac{\phi'(\theta E_-)\theta}{W^E} - \frac{I_-^2}{W^E} & \frac{W^I_-}{W^E} - \frac{2I_-(E_- - p)}{W^E} & -\frac{-I_- + \phi(\theta E_-)}{W^E} \\ W^E a(1 - 2E_-)(-I + \phi(\theta E_-)) & aI_-^2(E_- - p)(1 - 2E_-) & -a\left(1 - 2E_-\right) I_-(-I_- + \phi(\theta E_-)) \\ W^E a(1 - 2E_-)I_-(E_- - p) & \frac{a(1-2E_-)I_-^3(E_- - p)^2}{-I + \phi(\theta E_-)} & -I_-^2(E_- - p)a(1 - 2E_-) \end{pmatrix}$$

which yields the following characteristic polynomial after simplification:

$$c(\lambda) \quad = \quad \lambda\left(\lambda^2 + \lambda\frac{(\theta\phi'(\theta E_-)W^I_- + I_-^2)}{W^E} + (3\phi(\theta E_-) - 2I_-)(1 - 2E_-)(E_- - p)\right) \tag{39}$$

which yields the following possibilities depending on the two non-zero roots of this equation, σ_1, σ_2:

$$\begin{aligned} \text{folded saddle} &\quad \rightarrow \quad \sigma_1\sigma_2 < 0, \sigma_{1,2} \in \mathbb{R} \\ \text{folded node} &\quad \rightarrow \quad \sigma_1\sigma_2 > 0, \sigma_{1,2} \in \mathbb{R} \\ \text{folded focus} &\quad \rightarrow \quad \sigma_1\sigma_2 < 0, \sigma_{1,2} \in Im(\sigma_{1,2}) \neq 0 \end{aligned}$$

These conditions were evaluated numerically using the analytically determined roots of equation (39) over the (θ, W^E) parameter plane (see Figure 3). The fold point condition, given by (38) was resolved numerically using the MATLAB numerical solver fsolve for the point I_-.

Appendix C: Local Stability Analysis of Equilibria in N-node Coupled System

The Mean-Field Solution

Here, we will consider a simple-case where the N node system without self-coupling is also analytically resolvable for the Hopf-bifurcation. In particular, consider the following conditions:

$$W^E_{ii} = 0, \quad W^E_{ij} = \frac{W^E}{N^E - 1} = \bar{W}^E$$

These solutions correspond to the mean-field of the N_E nodes. Note that the equilibria of the system (4)-(5) are unchanged, independent of the conditions (40). However, under the mean-field conditions (40), the stability criterion are resolvable. In particular, suppose we reorder the $3N_E$ equations such that the first N_E equations correspond to E_i, the next N_E correspond to I_i, and the final N_E correspond to W^I_i. Then the Jacobian can be written block matrix form:

$$J = \begin{pmatrix} -\left(\frac{1}{\tau_1} + \frac{\bar{W}^E\phi'(\phi^{-1}(p))}{\tau_1}\right)\boldsymbol{I}_{N_E} + \frac{\bar{W}^E\phi'(\phi^{-1}(p))}{\tau_1}\mathbf{1}_{N_E} & -\frac{\overline{W}^I\phi'(\phi^{-1}(p))}{\tau_1}\boldsymbol{I}_{N_E} & -\frac{\bar{I}\phi'(\phi^{-1}(p))}{\tau_1}\boldsymbol{I}_{N_E} \\ \phi'(\theta p)\theta\boldsymbol{I}_{N_E} & -\boldsymbol{I}_{N_E} & \mathbf{0}_{N_E} \\ \frac{\bar{I}}{\tau_2}\boldsymbol{I}_{N_E} & \mathbf{0}_{N_E} & \mathbf{0}_{N_E} \end{pmatrix}$$

where $\boldsymbol{I}_{N_E}$, $\mathbf{1}_{N_E}$ and $\mathbf{0}_{N_E}$ denote the N_E identity matrix, and $N_E \times N_E$ matrices where all elements are 1 or 0, respectively. The characteristic polynomial is given by the following:

$$\begin{aligned}
C(\lambda) &= \det\begin{pmatrix} -\left(\frac{1}{\tau_1}+\frac{\bar{W}^E\phi'(\phi^{-1}(p))}{\tau_1}\right)\boldsymbol{I}_{N_E}+\frac{\bar{W}^E\phi'(\phi^{-1}(p))}{\tau_1}\boldsymbol{1}_{N_E}-\boldsymbol{I}_{N_E}\lambda & -\frac{\overline{W}^I\phi'(\phi^{-1}(p))}{\tau_1}\boldsymbol{I}_{N_E} & -\frac{\bar{I}\phi'(\phi^{-1}(p))}{\tau_1}\boldsymbol{I}_{N_E} \\ \phi'(\theta p)\theta\boldsymbol{I}_{N_E} & -\boldsymbol{I}_{N_E}(1+\lambda) & \boldsymbol{0}_{N_E} \\ \frac{\bar{I}}{\tau_2}\boldsymbol{I}_{N_E} & \boldsymbol{0}_{N_E} & -\boldsymbol{I}_{N_E}\lambda \end{pmatrix} \\
&= \det\left(-\left(\left[\frac{1}{\tau_1}+\frac{\bar{W}^E\phi'(\phi^{-1}(p))}{\tau_1}+\lambda\right]\lambda(\lambda+1)+\lambda\left[\frac{\bar{W}^I\phi'(\phi^{-1}(p))\phi(\theta p)\theta}{\tau_1}\right]+(\lambda+1)\bar{I}^2\frac{\phi'(\phi^{-1}(p))}{\tau_1\tau_2}\right)\boldsymbol{I}_{N_E}\right. \\
&+ \left.\lambda(\lambda+1)\frac{\bar{W}^E\phi'(\phi^{-1}(p))}{\tau_1}\boldsymbol{1}_{N_E}\right) \qquad (40) \\
&= \det\left(-\hat{Q}(\lambda)\boldsymbol{I}_{N_E}+\lambda(\lambda+1)\frac{\bar{W}^E\phi'(\phi^{-1}(p))}{\tau_1}\boldsymbol{1}_{N_E}\right)
\end{aligned}$$

where we have arrived at (40) by applying the matrix determinant identity:

$$\det\begin{pmatrix}\boldsymbol{A} & \boldsymbol{B}\\ \boldsymbol{C} & \boldsymbol{D}\end{pmatrix} = \det\left(\boldsymbol{A}-\boldsymbol{B}\boldsymbol{D}^{-1}\boldsymbol{C}\right)\det\boldsymbol{D}$$

To proceed, we will note the following:

$$\bar{W}^E\boldsymbol{1}_{N_E} = \bar{W}^E\boldsymbol{u}\boldsymbol{u}^T, \quad \boldsymbol{u} = \begin{pmatrix}1\\1\\\vdots\\1\end{pmatrix}$$

which allows us to use the rank-1 update to the determinant:

$$\det\left(\boldsymbol{A}+\boldsymbol{u}\boldsymbol{u}^T\right) = \left(1+\boldsymbol{u}^T\boldsymbol{A}^{-1}\boldsymbol{u}\right)\mathbf{det}(A)$$

yields the following:

$$\begin{aligned}
C(\lambda) &= (-1)^{N_E}\hat{Q}(\lambda)^{N_E}\left(1-\frac{\bar{W}^E\phi'(\phi^{-1}(p))}{\tau_1}\lambda(\lambda+1)\hat{Q}(\lambda)^{-1}\boldsymbol{u}^T\boldsymbol{u}\right) \\
&= (-1)^{N_E}\hat{Q}(\lambda)^{N_E-1}\left(\hat{Q}(\lambda)-N_E\left(\frac{W^E}{N_E-1}\right)\frac{\phi'(\phi^{-1}(p))\lambda(\lambda+1)}{\tau_1}\right) \\
&= (-1)^{N_E}\hat{Q}(\lambda)^{N_E-1}C_{SN}(\lambda)
\end{aligned}$$

where $C_{SN}(\lambda)$ is the characteristic polynomial for the single, recurrently coupled node. Our analysis of the dual-node case applies here and the stability of the N_E-node system under mean-field assumptions applies. The N_E node system under mean-field connectivity has identical solutions to the single node system.

The Normalized Excitatory Weight Solution

Finally, we will consider an arbitrary weight matrix, $\boldsymbol{W}^E$ with the only constraint being that

$$\sum_{j=1}^{N_E}\boldsymbol{L}_{ij}^{EE} = 1, \quad \boldsymbol{W}^{EE} = W^E\boldsymbol{L}^{EE}.$$

Note that the mean-field example previously considered is a special case of assumption (41). The assumption is required as it stabilizes the equilibria for $\boldsymbol{W}_i^I$ to $\boldsymbol{W}_i^I = \bar{W}^I$ for all $i = 1,2,\ldots N_E$ where $\bar{W}^I$ is the single-node equilibrium solution. Using a similar derivation procedure as before, the characteristic polynomial simplifies to:

$$\begin{aligned}
C(\lambda) &= \det\left(-\hat{Q}(\lambda)\boldsymbol{I}_{N_E}+\lambda(\lambda+1)\frac{\phi'(\phi^{-1}(p))}{\tau_1}\boldsymbol{W}^{EE}\right) \qquad (41) \\
\hat{Q}(\lambda) &= \lambda^3+\lambda^2\left(\frac{1}{\tau_1}+1\right)+\lambda\left(\frac{1}{\tau_1}+\frac{\overline{W^I}\phi'(\phi^{-1}(p))\phi'(\theta p)\theta}{\tau_1}+\frac{\bar{I}^2\phi'(\phi^{-1}(p))}{\tau_1\tau_2}\right)+\frac{\bar{I}^2\phi'(\phi^{-1}(p))}{\tau_1\tau_2}.
\end{aligned}$$

This implies that

$$
\begin{aligned}
C(\lambda) &= \det\left(\lambda(\lambda+1)\frac{\phi'(\phi^{-1}(p))}{\tau_1}\boldsymbol{W}^{EE} - \hat{Q}(\lambda)\boldsymbol{I}_{N_E}\right) \\
&= \det\left(q_0(\lambda)\boldsymbol{L}^{EE} - \hat{Q}(\lambda)\boldsymbol{I}_{N_E}\right), \quad q_0(\lambda) = \lambda(\lambda+1)\frac{\phi'(\phi^{-1}(p))}{\tau_1}W^E \\
&= q_0(\lambda)^{N_E}\det\left(\boldsymbol{L}^{EE} - \frac{\hat{Q}(\lambda)}{q_0(\lambda)}\boldsymbol{I}_{N_E}\right) \\
&= q_0(\lambda)^{N_E}\det\left(\boldsymbol{L}^{EE} - \mu I_{N_E}\right), \quad \mu = \frac{\hat{Q}(\lambda)}{q_0(\lambda)} \\
&= q_0(\lambda)^{N_E}\prod_{i=1}^{N_E}(\mu - r_i)
\end{aligned}
$$

where r_i are the eigenvalues of $\boldsymbol{L}^{EE}$. Undoing the substitutions resolves the factorized characteristic polynomial:

$$
C(\lambda) = \prod_{i=1}^{N_E}\left(\hat{Q}(\lambda) - r_i\frac{\lambda(\lambda+1)\phi'(\phi^{-1}(p))}{\tau_1}W^E\right)
$$

This factorization of $C(\lambda)$ allows one to resolve the Hopf bifurcation curve almost as easily as in the single node case. In particular, if all the eigenvalues are real (for example, if the matrix $\boldsymbol{W}^{EE}$ is symmetric) then the Hopf bifurcation curve occurs when a complex conjugate pair of roots of

$$
\hat{Q}(\lambda) - \frac{r_i\lambda(\lambda+1)\phi'(\phi^{-1}(p))W^E}{\tau_1}
$$

cross $\mathrm{Re}(\lambda_i) = 0$. For the experimentally derived weight matrix we consider, all eigenvalues of $\boldsymbol{W}^{EE}$ are real due to the near symmetric nature of the matrix ([Honey et al., 2009, Hellyer et al., 2016, Hagmann et al., 2008]). Thus, the potential Hopf-bifurcation curves are:

$$
\begin{aligned}
W^E_{Hopf,i}(\theta) &= \frac{1}{r_i\phi'(\phi^{-1}(p))}(1 - \tau_1\mu_+(\theta)) \\
\mu_\pm &= \frac{-(D(\theta) + F(\theta)\kappa(\theta) + 1 - \kappa(\theta)) \pm \sqrt{(F(\theta)\kappa(\theta) + D(\theta) + 1 - \kappa(\theta))^2 - 4\kappa(\theta)F(\theta)(1-\kappa(\theta)}}{2(1-\kappa(\theta))} \\
F(\theta) &= \frac{1 - r^{max}p^{-1}\phi^{-1}(p)\phi'(\phi^{-1}(p))}{\tau_1} \\
\kappa(\theta) &= \frac{p\phi'(\theta p)\theta}{\phi(\theta p)r^{max}} \\
D(\theta) &= \frac{\bar{I}^2\phi'(\phi^{-1}(p))}{\tau_1\tau_2}.
\end{aligned}
$$

This implies that as we increase W^E, the first transition through $W^E_{Hopf,i}(\theta)$ yields a Hopf bifurcation. Due to the form of (42), this is likely to correspond to the eigenvalue of $\boldsymbol{L}$, $\boldsymbol{r}^{max}$ with the largest positive real part. Finally, we remark that if the row sum of the weight matrix $\boldsymbol{L}^{EE}$ is not constant but narrowly distributed around a mean-value $\bar{L}$, than one can readily derive the following approximation:

$$
\begin{aligned}
W^E_{Hopf,i}(\theta) &\approx \frac{1}{r^{max}\phi'(\phi^{-1}(p))}(1 - \tau_1\mu_+(\theta)) && (42) \\
r^{max} &= \max_{i=1\ldots N_E}\{r_i\} && (43) \\
F(\theta) &= \left(1 - \frac{r^{max}}{\bar{L}}p^{-1}\phi^{-1}(p)\phi'(\phi^{-1}(p))\right) && (44) \\
\kappa(\theta) &= \frac{p\phi'(\theta p)\theta\bar{L}}{\phi(\theta p)r^{max}} && (45)
\end{aligned}
$$

which we apply to the coupling matrix from [Hellyer et al., 2016] where $\bar{L} = 0.2318$ and $r^{max} = 0.3148$.

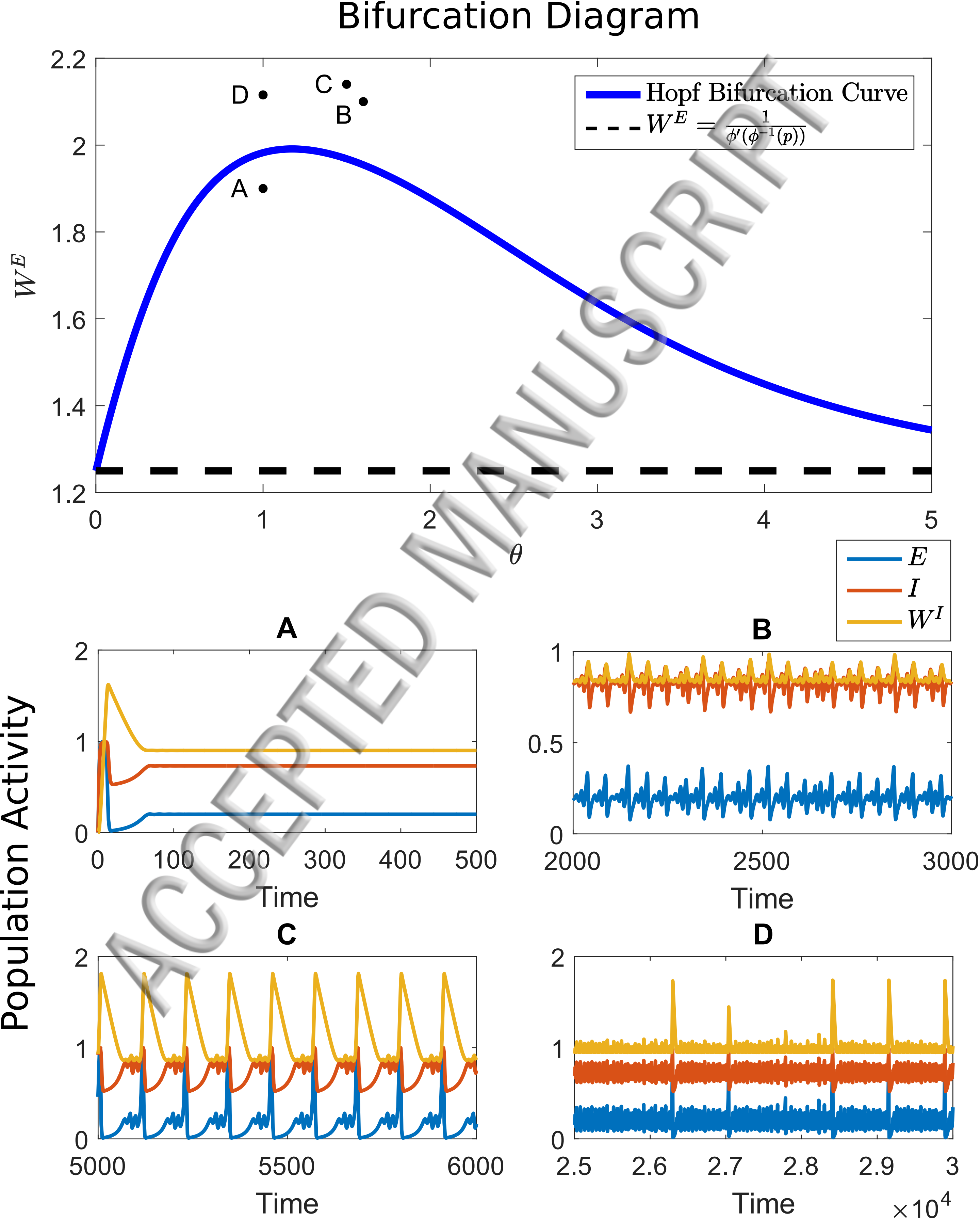
Bifurcation Diagram
Hopf Bifurcation Curve
$W^E = \frac{1}{\phi'(\phi^{-1}(p))}$
W^E
θ
2.2
2
1.8
1.6
1.4
1.2
0
1
2
3
4
5
A
B
C
D
Population Activity
E
I
W^I
A
2
1
0
0
100
200
300
400
500
Time
B
1
0.5
0
2000
2500
3000
Time
C
2
1
0
5000
5500
6000
Time
D
2
1
0
2.5
2.6
2.7
2.8
2.9
3
Time
$\times 10^4$

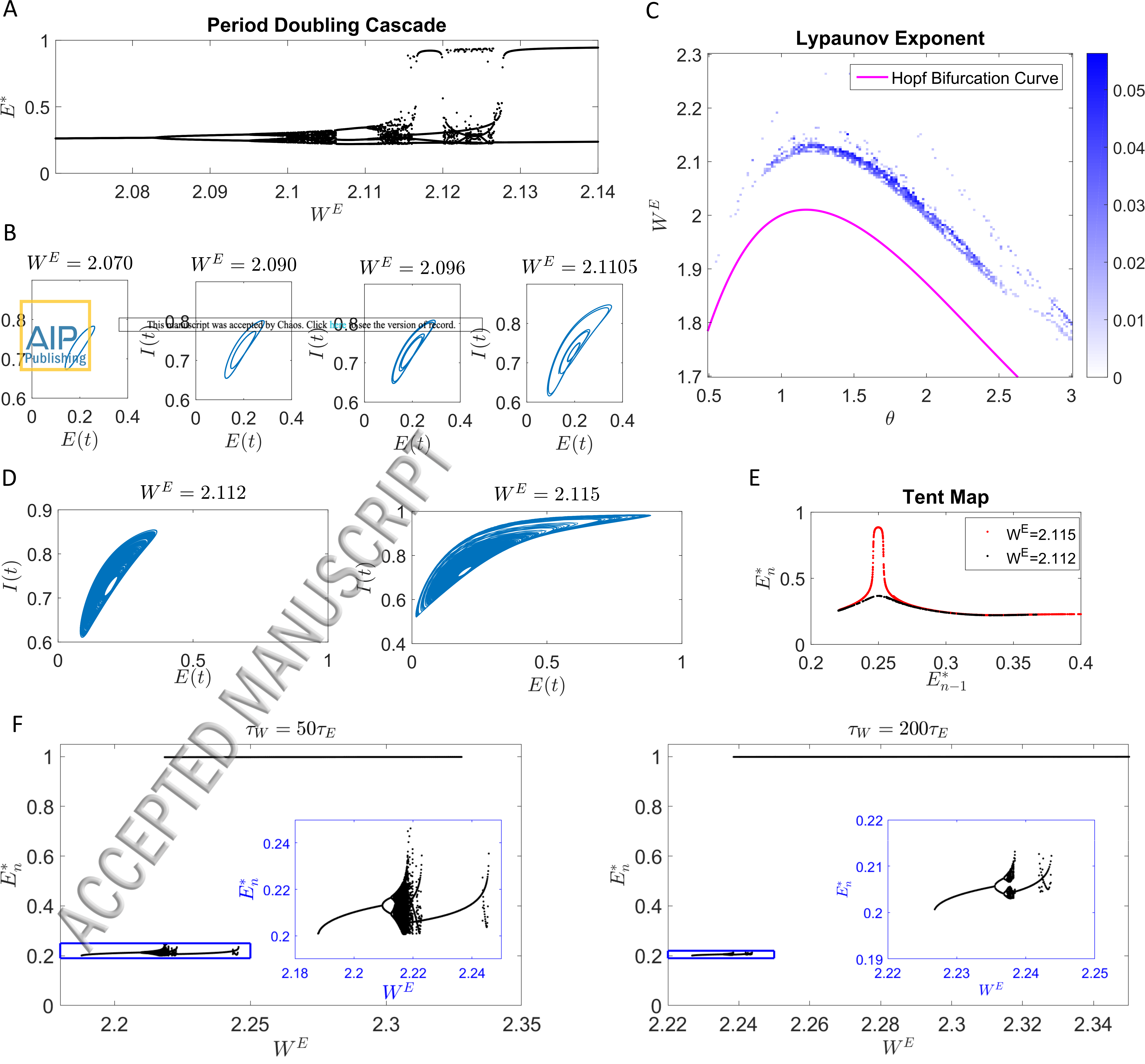
A
Period Doubling Cascade
E^*
W^E
B
$W^E = 2.070$
$W^E = 2.090$
$W^E = 2.096$
$W^E = 2.1105$
$I(t)$
$E(t)$
C
Lypaunov Exponent
Hopf Bifurcation Curve
W^E
θ
D
$W^E = 2.112$
$W^E = 2.115$
$I(t)$
$E(t)$
E
Tent Map
W^E=2.115
W^E=2.112
E^*_n
E^*_{n-1}
F
$\tau_W = 50\tau_E$
$\tau_W = 200\tau_E$
E^*_n
W^E

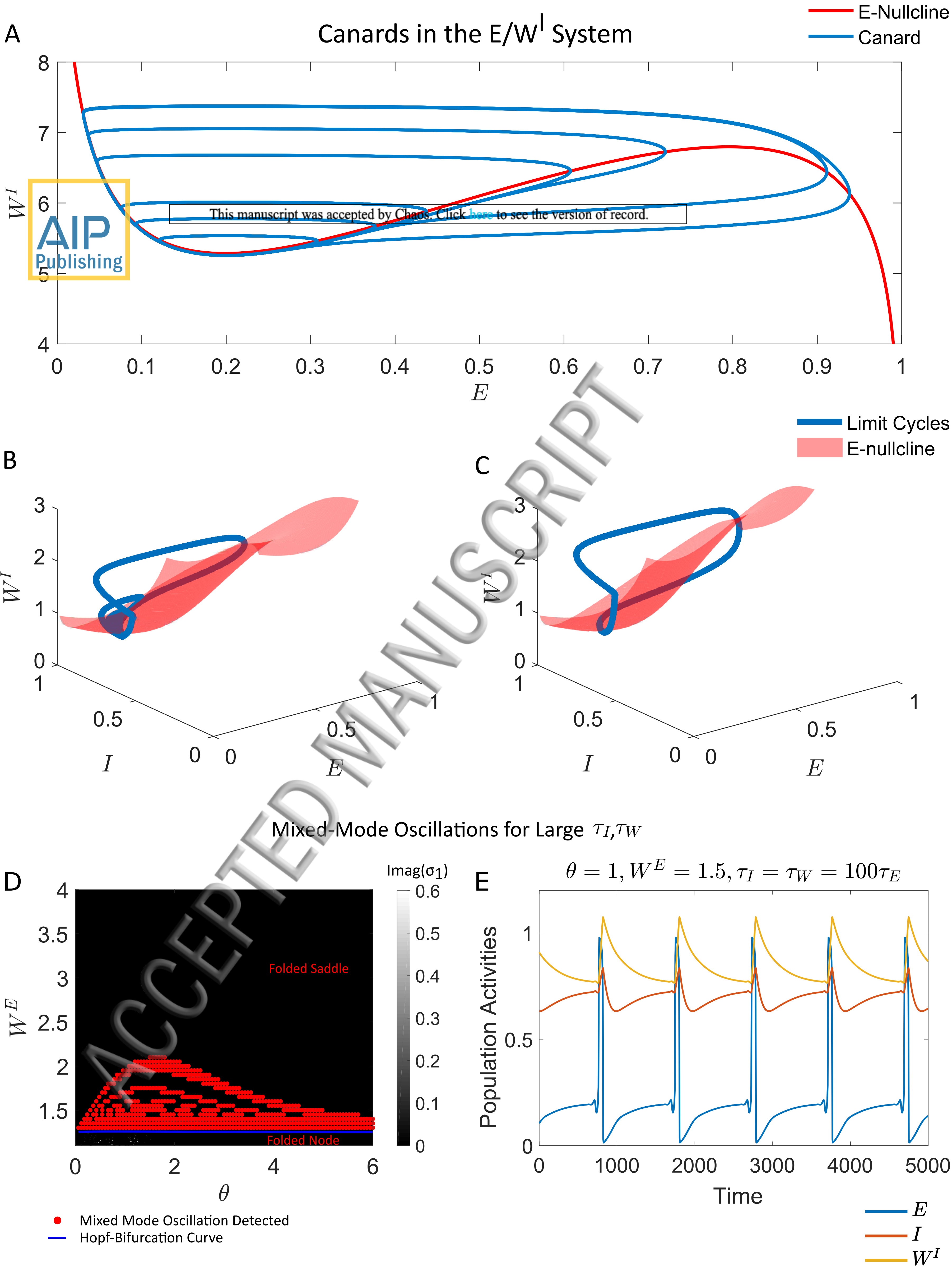
A
Canards in the E/W^I System
E-Nullcline
Canard
W^I
8
7
6
5
4
0
0.1
0.2
0.3
0.4
0.5
0.6
0.7
0.8
0.9
1
E
Limit Cycles
E-nullcline
B
C
3
2
1
0
W^I
1
0.5
0
I
0
0.5
1
E
Mixed-Mode Oscillations for Large τ_I,τ_W
D
Imag(σ1)
0.6
0.5
0.4
0.3
0.2
0.1
0
4
3.5
3
2.5
2
1.5
W^E
Folded Saddle
Folded Node
0
2
4
6
θ
Mixed Mode Oscillation Detected
Hopf-Bifurcation Curve
E
$\theta = 1, W^E = 1.5, \tau_I = \tau_W = 100\tau_E$
Population Activities
1
0.5
0
0
1000
2000
3000
4000
5000
Time
E
I
W^I

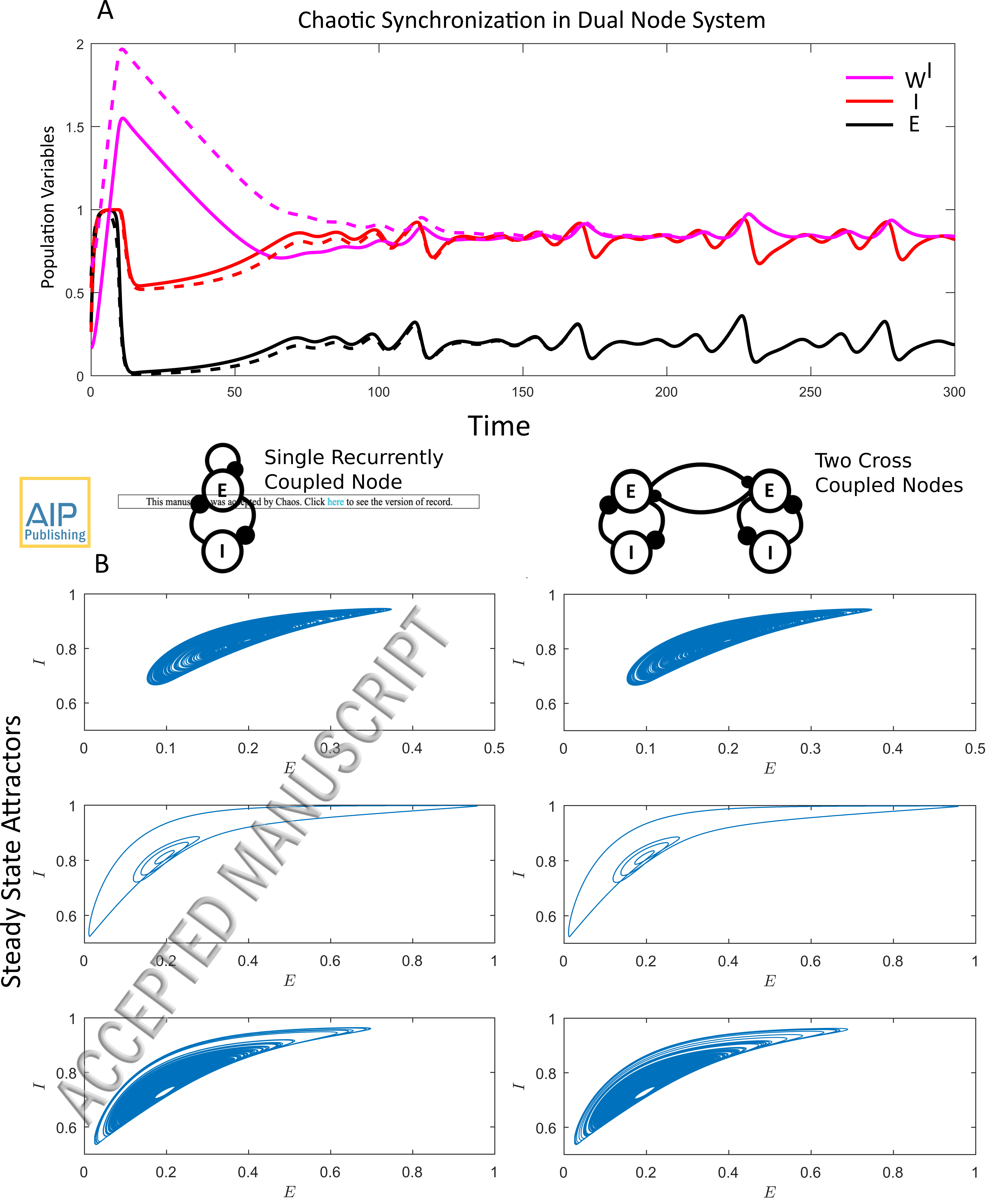
A
Chaotic Synchronization in Dual Node System
Population Variables
Time
0
0.5
1
1.5
2
0
50
100
150
200
250
300
W^I
I
E
Single Recurrently Coupled Node
Two Cross Coupled Nodes
E
I
B
Steady State Attractors
I
E
0.6
0.8
1
0
0.1
0.2
0.3
0.4
0.5
0.2
0.4
0.6
0.8

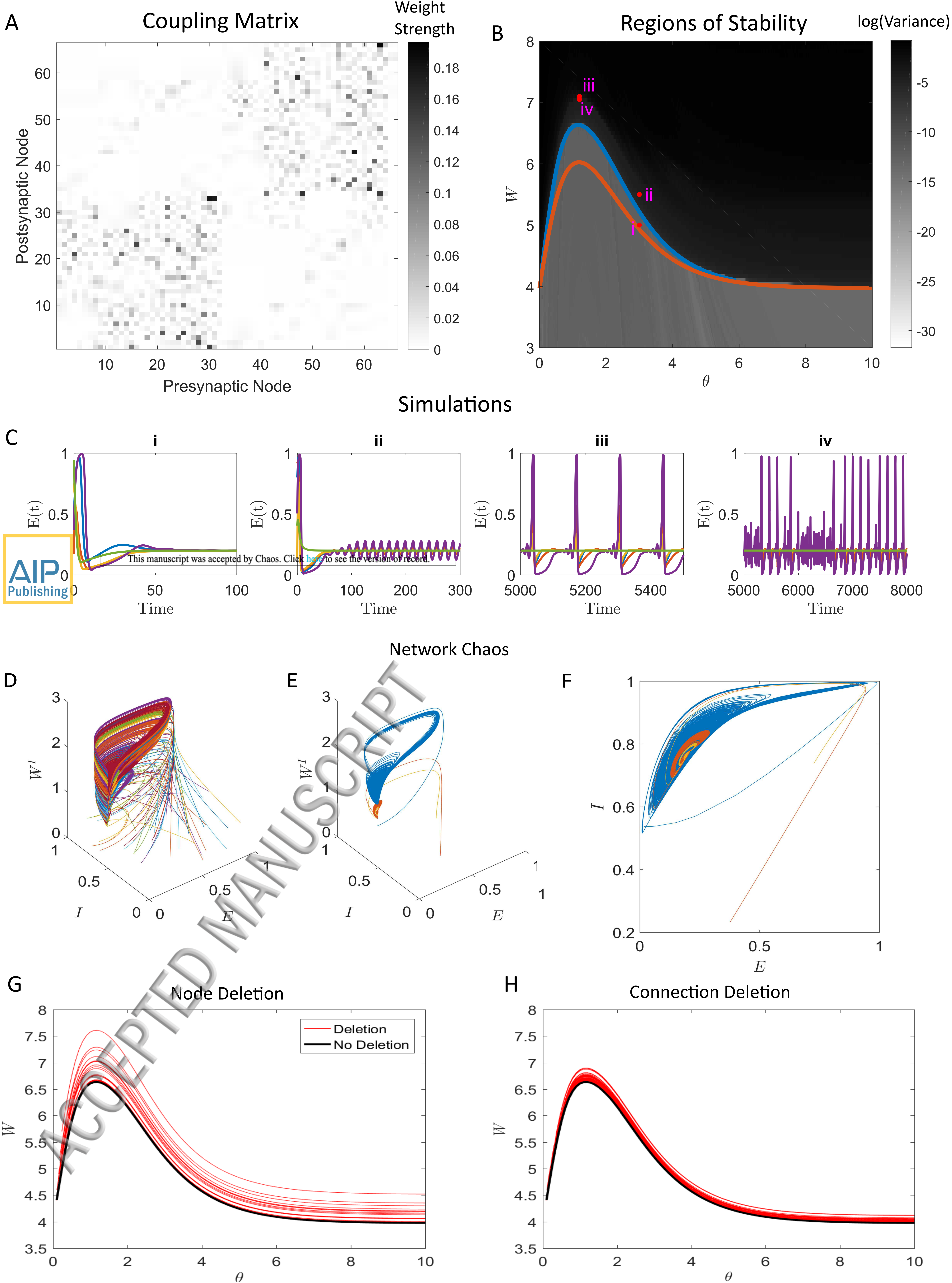
A
Coupling Matrix
Weight Strength
Postsynaptic Node
Presynaptic Node
0.18
0.16
0.14
0.12
0.1
0.08
0.06
0.04
0.02
0
B
Regions of Stability
log(Variance)
-5
-10
-15
-20
-25
-30
W
θ
i
ii
iii
iv
Simulations
C
i
ii
iii
iv
E(t)
Time
Network Chaos
D
E
F
W^I
I
E
G
Node Deletion
Deletion
No Deletion
H
Connection Deletion
W
θ